CAL-2284

National Aeronautics and Space Administration

ROSAT

ANNUAL STATUS REPORT

FOR NASA GRANT NAG 5-1935

Submitted by: The Trustees of Columbia University
in the City of New York
Box 20, Low Memorial Library
New York, New York 10027

Prepared by: Columbia Astrophysics Laboratory
Departments of Astronomy and Physics
Columbia University
538 West 120^{th} Street
New York, New York 10027

Title of Research: **"ROSAT Observation Program"**

Principal Investigator: Jules P. Halpern
Associate Professor of Astronomy

Period Covered by Report: 1 November 1993 – 31 October 1994

March 1995

TABLE OF CONTENTS

1. SURFACE EMISSION OF THE GEMINGA PULSAR

1.1. Summary

The Geminga pulsar was observed by the *ROSAT* PSPC for 37,000 s in September 1993, in order to make a more detailed study than was possible previously of the pulse profile and two-component spectrum, and to do phase-resolved spectroscopy. This exposure was 2.5 times longer than the original discovery observation. In addition, a shorter 4,000 s exposure was made in October 1992, simultaneously with a GRO observation of Geminga, in order to verify the absolute phasing of the X-ray and γ-ray peaks.

We verified that the spectrum can be described as the sum of two black bodies, whose temperatures are 6×10^5 K and $3 - 4 \times 10^6$ K, with the latter covering 3×10^{-5} the area of the former. The pulse profiles indicate that the intensity of the two emitting regions peak $\sim 90°$ out of phase in rotation, but that the temperatures are otherwise independent of phase. An improved estimate of the distance can be made from the cooler (larger) blackbody component, yielding $d = 440 \pm 120$ pc.

1.2. Pulse Profiles and Timing

The pulse profiles of the three PSPC observations of Geminga are shown in Figures 1, 2, and 3. In each Figure, the top panel represents the full energy band over which photons are detected, and the lower three panels are the same data broken into three different energy bands. The October 1992 and September 1993 profiles are basically consistent with the orginal (March 1991) data as published by Halpern & Holt (1992) and Halpern & Ruderman (1993). The latest observation affords the most detailed look are the light curve. The soft bands, 0.08–0.28 keV and 0.28–0.53 keV, have roughly the same pulse profiles and pulsed fractions, while the 0.5–1.5 keV data are dramatically different. Above 0.5 keV, the phase of the peak changes by about 90°, and the pulsed fraction approaches 100%. These results are consistent with our original interpretation, namely, that the inclination angle

of the magnetic dipole is large, and that the two hot polar caps are close together on the surface of the star so that they present only one pulse peak per rotation. However, there is still no explanation for the shape and phase offset of the lower-energy data, which must be coming from a large fraction of the surface of the neutron star. A preliminary attempt at pulse phase spectroscopy using this latest observation is described in the next section.

All three PSPC observations of Geminga were corrected to the Solar System barycenter using the latest version of the timing rountines in PROS (2.3.1). Using the most recent and accurate EGRET ephemeris (Mattox 1994), we have verified that the three ROSAT light curves maintain the same pulse-phase relationship over the 2.5 year interval between March 1991 and September 1993. However, there seems to be an offset of 1 second in the 1993 timing because the leap second of July 1, 1993 was not added in the PROS barycentering code. We must add this 1 second in order for the latest observation to phase correctly with the previous two, and we assume that this is the correct solution of the problem. The absolute phase with respect to the γ-ray pulse is still uncertain because the ROSAT times are expressed in UTC, rather the TDB (Barycentric Dynamical Time) in which pulsar ephemerides are usually expressed. We are currently checking (with the help of Frank Primini) the reliability of the PROS barycentering code, the accuracy of the ROSAT spacecraft clock, and will convert the photon times to TDB if it seems that this can be done reliably.

1.3. PSPC Spectra

The PSPC spectra can only be fit by a two-component model. We have considered two types of models. One consists of a pair of blackbodies, and the other consists of a black body plus a a power-law. These models fit equally well to within the expected errors, and much tighter limits on the parameters are obtained with the most recent long exposure than were possible with the original, published data. The best fits are shown in Figures 4 and 5. In both cases, we have searched the the full four-dimensional Chi-square grids

(e.g., $T_1, T_2 N_{\rm H}, A_2/A_1$) to derive errors on the spectral parameters. Figure 6 shows the confidence limits for the soft blackbody temperature T_1 and $N_{\rm H}$. Figure 6a is the result for the double blackbody model, and Figure 6b is for the blackbody plus power-law. The temperature is either $6.1 \pm 0.5 \times 10^5$ K, or $5.6 \pm 0.8 \times 10^5$ K, depending on which model is chosen. In both cases, the derived column density is close to 1.0×10^{20} cm^{-2}, which is consistent with the measurments of $N_{\rm H}$ in this direction to stars at distances of several hundred parsecs.

An independent estimate of the distance can be derived by assuming that the soft blackbody component comes from the full surface of a neutron star of radius 10 km and making use of the normalization constants in the spectral fits. The resulting contours of equal distance are shown in Figure 6. In the case of the double blackbody fit, a distance of 440 ± 120 pc is indicated. This is slightly larger than, but consistent with our published estimate of 250 ± 150 pc based on the original data. For the blackbody plus power-law fit, a slightly smaller distance of 350 ± 150 pc is found. Either of these results are consistent with the proper motion of Geminga as compared to typical velocites of pulsars (Lyne & Lorimer 1994), and support the model in which Geminga is a highly efficient γ-pulsar emitting by the outer gap mechanism. In fact, Yadigaroglu & Romani (1995) have independently come up with an independent, theoretical estimate of 400 pc based on such a model.

Figure 7 shows the confidence contours for the properties of the harder blackbody component. The temperature is $3.8 \pm 0.7 \times 10^6$ K, and the fractional area occupied by this component is only $\sim 3 \times 10^{-4}$ of the surface. This is ~ 10 times smaller than would be expected for the open-field line polar cap region, which indicates that the heating mechanism is probably not effective along the full open field-line bundle. Alternatively, the harder component may be represented by a power-law. Fits to this model indicate that the power-law energy index is 1.0 ± 0.4.

1.4. Phase-Resolved Spectroscopy

We have made a preliminary attempt at calculating spectra for particular rotation phases. A detailed application of this analysis is still in progress. The folded data were first divided into five phase bins, as shown in Figure 8 (the total data set for the September 1993 observation). Then the five individual pulse height spectra were normalized by their effective exposure times, and divided by the average spectrum. The resulting "ratio" spectra are displayed in Figure 9. Any change in the soft blackbody temperature with rotation phase would make itself evident as a change in slope of the points between 0.1 and 0.5 keV. It can be seen that the temperature is roughly constant with phase, with perhaps a slight decrease in phase bins 1 and 5 where the intensity is smallest, and a slight increase in the other phase bins. This is consistent with a model in which the modulation of the soft blackbody component is due to small differences in temperature over the surface of the star. This will be tested further with detailed spectral fitting. The statistics are poor on the harder component because it contains few photons, even in the summed spectrum. Nevertheless, the temperature at harder energies appears to be greatest in phase bin 2, which contains the peak of the hard component (since it leads the soft pulse by about 90°. Overall, the spectra and pulse profiles appear consistent with our two-temperature model, in which rotation is responsible for carrying the emission regions in and out of view without greatly changing their apparent temperatures.

2. NARROW-LINE SEYFERTS WITH PERMITTED FE II EMISSION

The purpose of this program is to obtain PSPC spectra of an important class of Seyfert galaxies which have narrow lines and strong permitted Fe II emission. Sometimes called I Zw 1 objects, or narrow-line Seyfert 1s, they are crucial to our understanding of Seyfert classification and models of Seyfert unification. Previous to the ROSAT observations, only three of these objects (I Zw 1, Mkn 957, and Mkn 507) had *Einstein* X-ray data (Halpern & Oke 1987). We observed four new objects, and in addition obtained data on 17 more from the ROSAT archive. The basic properties of these objects are listed in Table 1, and a log of their ROSAT observations is given in Table 2. The results of our spectral fits to simple power-law models, which provide adequate fits in most cases, are described in Table 3. A selection of XSPEC spectral fits and residuals are shown in Figures 11–23.

Most notably, we have found that even though they have narrow emission lines like Seyfert 2 galaxies, the X-ray luminosities of I Zw 1 objects are typical of Seyfert 1s. In addition, their spectra are significantly softer than those of either Seyfert 1 or Seyfert 2 galaxies, showing no evidence for absorption or scattering. In fact, they are often rapidly variable in X-rays, which proves that we have a direct and not a hidden view of their nuclei. Figure 10 shows a light curve of Mkn 957 (=5C 3.100), which displays a rapid dip in flux near the end of the observation.

These results are even more paradoxical in view of the fact that I Zw 1 objects usually have a high ratio of far-infrared to bolometric luminosity, which would be interpreted as evidence for a large covering fraction of obscuring material. We have also found a number of new such objects in the ROSAT/IRAS All-Sky Survey (Moran et al., in press). We are investigation possible correlations between X-ray spectral slope and either Balmer-line width or Fe II line equivalent width (Forster et al., in preparation).

3. DIFFUSE EMISSION AND PATHOLOGICAL SEYFERT SPECTRA

This program combines PSPC and HRI observations of selected Seyfert galaxies which have unusual and vraiable spectra. The purpose is to disentangle diffuse X-ray emission from the nuclear source, in order to properly interpret the soft X-ray spectral shapes in terms of partial covering and/or warm-absorber models. The targets in the program are NGC 3516, NGC 3227, and NGC 7314. So far, we have performed a detailed analysis only on NGC 3516, and we summarize the results here.

NGC 3516 is historically the Seyfert galaxy with the highest degree of soft X-ray variability. In addition to intrinsic variability of at least a factor of 30, the apparent column density has ranged from $> 10^{24}$ to essentially zero. NGC 3516 also displays variable UV absorption lines of the type that are sometimes though of as low-velocity analogues of the same phenomenon in BAL QSOs. Figure 24 is our PSPC light curve, which indicates that there was variabilty of about 25% in one day. The power-law spectral fit displayed in Figure 25 shows the classic signature of deviations due to a warm absorber. Indeed, a fit to a warm-absorber model (Figure 26) is a good fit, with an edge of optical depth 0.9 at 0.75 keV that can be attributed to O VII with a column density of 4×10^{18}, equivalent to a hydrogen column of 5.7×10^{21}. Otherwise, there is no significant cold column above the Galactic value of 3×10^{20}. Dividing the data into high and low states (Figures 27 and 28) reveal no significant differences in the parameters of the absorption edge, as the overlapping confidence contours in Figures 29 and 30 demonstrate. Given that the intensity changed by only 25%, it is not surprising that the properties of the warm absorber remained roughly the same.

We plan to combine these data with historical X-ray spectra and ASCA spectrum that we have also obtained, in order to specify the state of the warm absorber, and relate it to the UV absorption lines and large-amplitude historical X-ray variability.

4. NGC 1672: THE SECOND BRIGHTEST SEYFERT GALAXY

This object is a nearby, southern Seyfert 2 galaxy, and one of the original "composite" Seyfert/starburst galaxies which have evidence for both Seyfert activity and H II regions in their optical spectra. It is one of the lowest luminosity Seyfert 2 galaxies that can be studied in detail. We have obtained both PSPC and HRI observations in order to disentangle the emission from nuclear and starburst activity, both spectrally and spatially. The analysis is still in its early stages, but we do see both nuclear and off-nuclear sources. Figure 31 shows the HRI imgage in which the nulear source is the strongest, although it is possibly extended. In addition, there are discrete sources straddling the nucleus in the east-west direction that are probably associated with the star-forming bar that is also oriented in this direction. All of these sources are detected in the PSPC as well, and we plan to do a spatial and spectral analysis of their separate properties.

Table 1. Narrow Line Seyfert Galaxy Sample

Name	Other Name	J2000 Coordinates α	δ	z^a	Class
Mkn 335	PG 0003+199	00 06 19.5	20 12 10.4	0.0260	Sey 1
Mkn 957	5C 03.100	00 41 53.4	40 21 17.4	0.0738[2]	Sey 1
I Zw 1	PG 0050+124	00 53 34.9	12 41 36.2	0.0627	Sey 1
Mkn 359	IRAS 01248+1855	01 27 32.5	19 10 43.8	0.0168[1]	Sey 1.5
PHL 1092	Q 0137+060	01 39 55.8	06 19 21.3	0.396[1]	QSO ?
Mkn 1044	IRAS F02276-0913	02 30 05.4	-08 59 52.5	0.0166	Sey 1
Mkn 1239	IRAS 09497-0122	09 52 19.1	-01 36 43.4	0.0196	Sey 1
Mkn 42	IRAS F11510+4629	11 53 41.7	46 12 42.1	0.0243	Sy 1
PG 1244+026	IRAS F12440+0238	12 46 35.2	02 22 08.3	0.048[1]	Sey 1
IRAS 13224-3809		13 25 21.1	-38 24 41.0	0.0667[1]	Sey 1
PG 1404+226		14 06 21.9	22 23 46.6	0.098[1]	??
Mkn 478	PG 1440+356	14 42 07.5	35 26 22.9	0.0828	Sey 1
Mkn 486	PG 1535+547	15 36 38.3	54 33 33.2	0.0389	Sey 1
PG 1543+489	IRAS F15439+4855	15 45 30.2	48 46 08.9	0.400[1]	QSO ?
Mkn 291	IRAS F15529+1920	15 55 07.9	19 11 32.8	0.0352	Sey 1
Mkn 493	IRAS 15572+3510	15 59 09.6	35 01 47.5	0.0321	Sey 1
IRAS 16319+4725		16 33 23.0	47 19 03.4	0.1163[1]	??
IRAS 17020+4544		17 03 30.3	45 40 50.3	0.0604[1]	Sey 2
1747.3+6836	VII Zw 742	17 46 59.6	68 36 28.4	0.063[1]	Sey 1
Mkn 507	IRAS 17489+6843	17 48 38.3	68 42 15.9	0.0559[1]	Sey 2
Mkn 896	IRAS 20437-0259	20 46 20.8	-02 48 45.2	0.0265	Sey 1

[a] Redshifts have been obtained recession velocities using the expression:

$$1 + z = [(c + V)/(c - V)]^{0.5}$$

[1] From RC3. [2] $z=\Delta\lambda/\lambda$ was given in Burbidge (1970). [3] Redshifts adapted from observations of USS X-ray Survey AGN, Puchnarewicz *et al* 1992.

Table 2. ROSAT Observation Log

Name	Seq ID	PI	Date	Exposure[a]	CTR[b]
Mkn 335	rp700101	Turner	1991 June 29 - 30	24586	1.721
Mkn 957	wp600079	Truemper	1991 July 14 - 15	42164	0.075
I Zw 1	wp700260	Lawrence	1991 Dec 31	3505	0.799
Mkn 359	wp701220	Mittaz	1992 July 15	3189	0.787
PHL 1092	wp700259	Lawrence	1992 Jan 19 - 22	7786	0.283
Mkn 1044	rp700792	Halpern	1992 Aug 9 - 10	2830	2.073
Mkn 1239	rp700908	Malkan	1992 Nov 8	9051	0.067
Mkn 42	rp700791	Halpern	1992 Dec 4 - 5	4433	0.229
PG 1244+026	rp700020	Elvis	1991 Dec 22 - 24	5566	1.000
IRAS 13224-3809	wp600419	Boller	1992 Aug 10 - 12	20136	0.324
PG 1404+226	wp700227	Ulrich	1991 July 11 - 12	10141	0.301
Mkn 478	wp700559	Gondhalekar	1992 Jan 17	2393	2.004
Mkn 486	wp701196	Meurs	1993 Feb 8	2792	0.066
PG 1543+489	rp700808	Laor	1992 Aug 22 - 23	7181	0.115
Mkn 291	wp300167	Mason	1992 Feb 27	3816	0.066
Mkn 493	rp700096	Halpern	1992 Feb 1 - 29	8172	0.352
IRAS 16319+4725	wp701549	Bade	1993 July 24	3880	0.240
IRAS 17020+4544	wp701153	Meurs	1992 Aug 28	2644	0.774
1747.3+6836	wp701523	Boller	1993 Aug 8 - 10	24754	0.274
Mkn 507	wp701523	Boller	1993 Aug 8 - 10	24754	0.033
Mkn 896	rp700793	Halpern	1992 Nov 10 - 1993 Apr 22	9587	0.443

[a]Total accepted time in seconds.

[b]Count Rate, background subtracted, in counts s^{-1} through PI channels 3-34 (see §2).

Table 3. Best Fit Spectral Parameters for Powerlaw Models and Estimated Luminosities

Name	Γ	N_H (10^{20} cm^{-2})	$N_{H\ (Stark)}$[a] (10^{20} cm^{-2})	A[b] (10^{-3}) (ph cm^{-2} s^{-1} keV^{-1})	χ^2_{min}	$F^c_{(0.1-2.5keV)}$ (10^{-12}) (erg cm^{-2} s^{-1})	$L_{(0.1-2.5keV)}$ (10^{43}) (erg s^{-1})
Mkn 335[1]	$3.073\ ^{+0.069}_{-0.067}$	$4.05\ ^{+0.19}_{-0.19}$	3.98	6.61 ± 0.06	2.812	25.15	7.43
Mkn 957[1]	$2.913\ ^{+0.338}_{-0.316}$	$^{**}9.77\ ^{+2.25}_{-1.67}$	6.25	0.56 ± 0.03	0.255	1.28	2.92
I Zw 1	$3.045\ ^{+0.294}_{-0.286}$	$^{*}6.89\ ^{+1.01}_{-0.94}$	[2]5.50	3.45 ± 0.11	0.360	9.82	16.09
Mkn 359	$2.425\ ^{+0.307}_{-0.301}$	$5.14\ ^{+1.06}_{-0.98}$	5.55	3.44 ± 0.12	0.394	9.56	1.17
PHL 1092	$4.164\ ^{+0.626}_{-0.496}$	$4.13\ ^{+1.41}_{-1.09}$	3.93	0.25 ± 0.05	0.472	1.95	185.78
Mkn 1044	$2.996\ ^{+0.202}_{-0.190}$	$^{*}3.94\ ^{+0.56}_{-0.54}$	3.04	5.36 ± 0.14	0.847	19.95	2.39
Mkn 1239	$3.885\ ^{+1.068}_{-0.923}$	$^{*}8.10\ ^{+3.41}_{-2.89}$	3.98	0.23 ± 0.04	0.225	0.83	0.14
Mkn 42	$2.634\ ^{+0.700}_{-0.564}$	$2.44\ ^{+1.78}_{-1.25}$	1.90	0.50 ± 0.07	0.259	1.94	0.50
PG 1244+026	$3.212\ ^{+0.256}_{-0.234}$	$^{*}2.66\ ^{+0.59}_{-0.50}$	1.81	1.38 ± 0.07	0.404	7.06	7.27
IRAS 13224-3809	$4.297\ ^{+0.218}_{-0.212}$	$^{**}8.44\ ^{+0.68}_{-0.66}$	5.77	0.90 ± 0.03	1.635	3.97	8.04
PG 1404+226[1]	$3.353\ ^{+0.396}_{-0.337}$	$2.84\ ^{+0.96}_{-0.76}$	2.07	0.38 ± 0.04	1.169	2.07	9.29
Mkn 478	$3.447\ ^{+0.286}_{-0.250}$	$^{*}1.57\ ^{+0.41}_{-0.34}$	1.01	1.79 ± 0.16	0.391	14.68	42.28
Mkn 486	$2.350\ ^{+4.510}$	$1.46\ ^{+9.98}$	1.37	0.14 ± 0.11	0.175	0.54	0.36
PG 1543+489	$3.643\ ^{+1.330}_{-0.817}$	$3.02\ ^{+2.63}_{-1.54}$	1.60	0.12 ± 0.05	0.362	0.75	71.88
Mkn 291	$2.594\ ^{+4.609}$	$2.90\ ^{+11.5}$	3.46	0.24 ± 0.14	0.221	0.86	0.47
Mkn 493	$2.813\ ^{+0.383}_{-0.338}$	$2.73\ ^{+0.93}_{-0.75}$	2.02	0.73 ± 0.05	0.348	2.94	1.33
IRAS 16319+4725	$2.488\ ^{+0.666}_{-0.485}$	$0.63\ ^{+0.86}_{-0.56}$	1.61	0.26 ± 0.08	0.346	1.34	8.56
IRAS 17020+4544	$2.385\ ^{+0.364}_{-0.339}$	$3.35\ ^{+1.01}_{-0.88}$	2.25	2.60 ± 0.11	0.421	8.26	13.41
1747.3+6836	$2.587\ ^{+0.177}_{-0.172}$	$3.86\ ^{+0.52}_{-0.48}$	4.31	0.95 ± 0.02	0.884	3.04	5.39
Mkn 507	$1.475\ ^{+0.732}_{-0.678}$	$3.22\ ^{+3.38}_{-2.16}$	4.42	0.15 ± 0.02	0.436	0.44	0.59
Mkn 896	$2.567\ ^{+0.258}_{-0.246}$	$3.35\ ^{+0.74}_{-0.65}$	4.74	1.33 ± 0.04	0.537	4.46	1.37

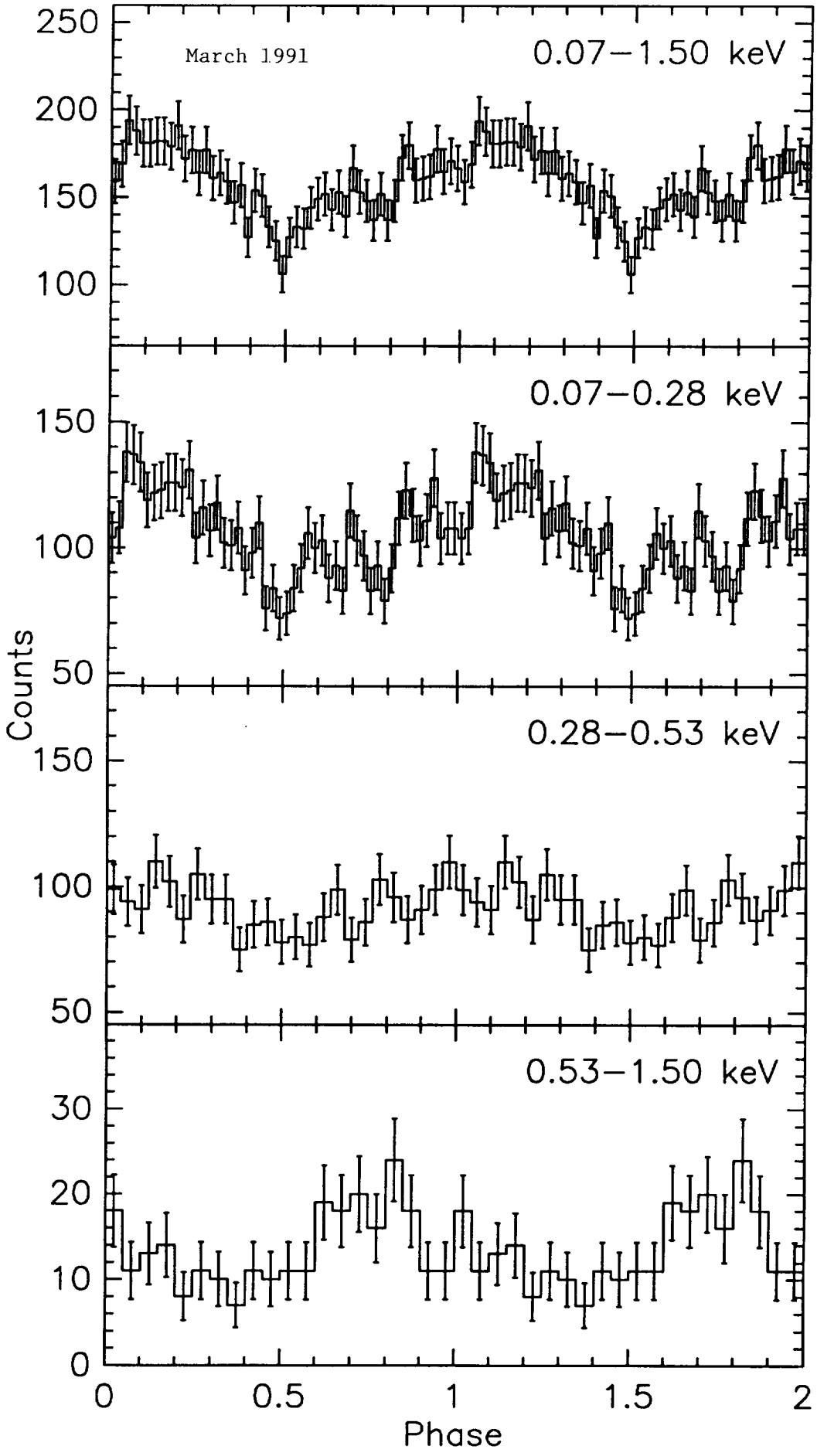
March 1991
0.07–1.50 keV
0.07–0.28 keV
0.28–0.53 keV
0.53–1.50 keV
Counts
Phase
250
200
150
100
150
100
50
150
100
50
30
20
10
0
0
0.5
1
1.5
2

Fig. 1

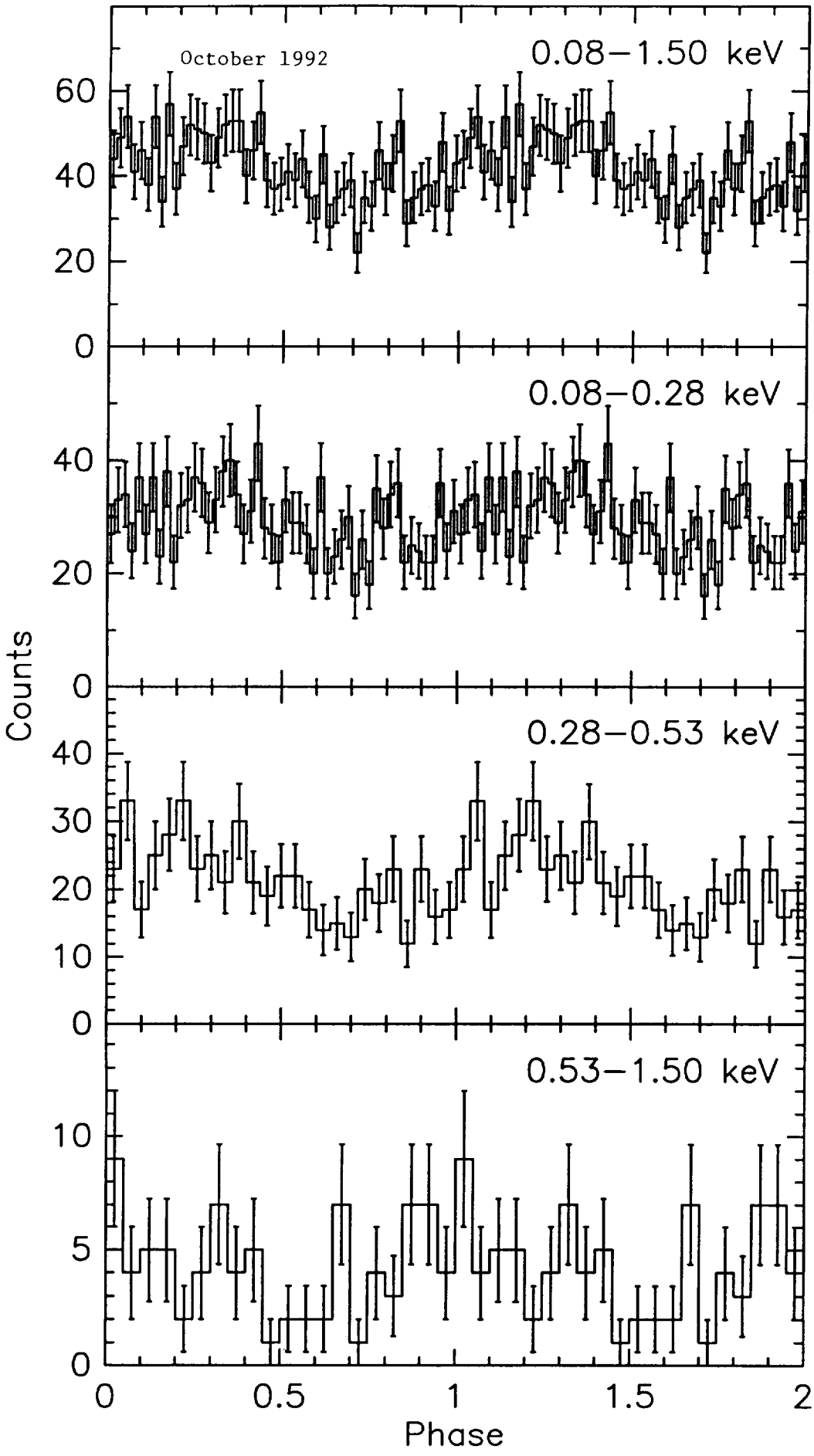
October 1992
0.08–1.50 keV
0.08–0.28 keV
0.28–0.53 keV
0.53–1.50 keV
Counts
Phase
0
0.5
1
1.5
2

Fig. 2

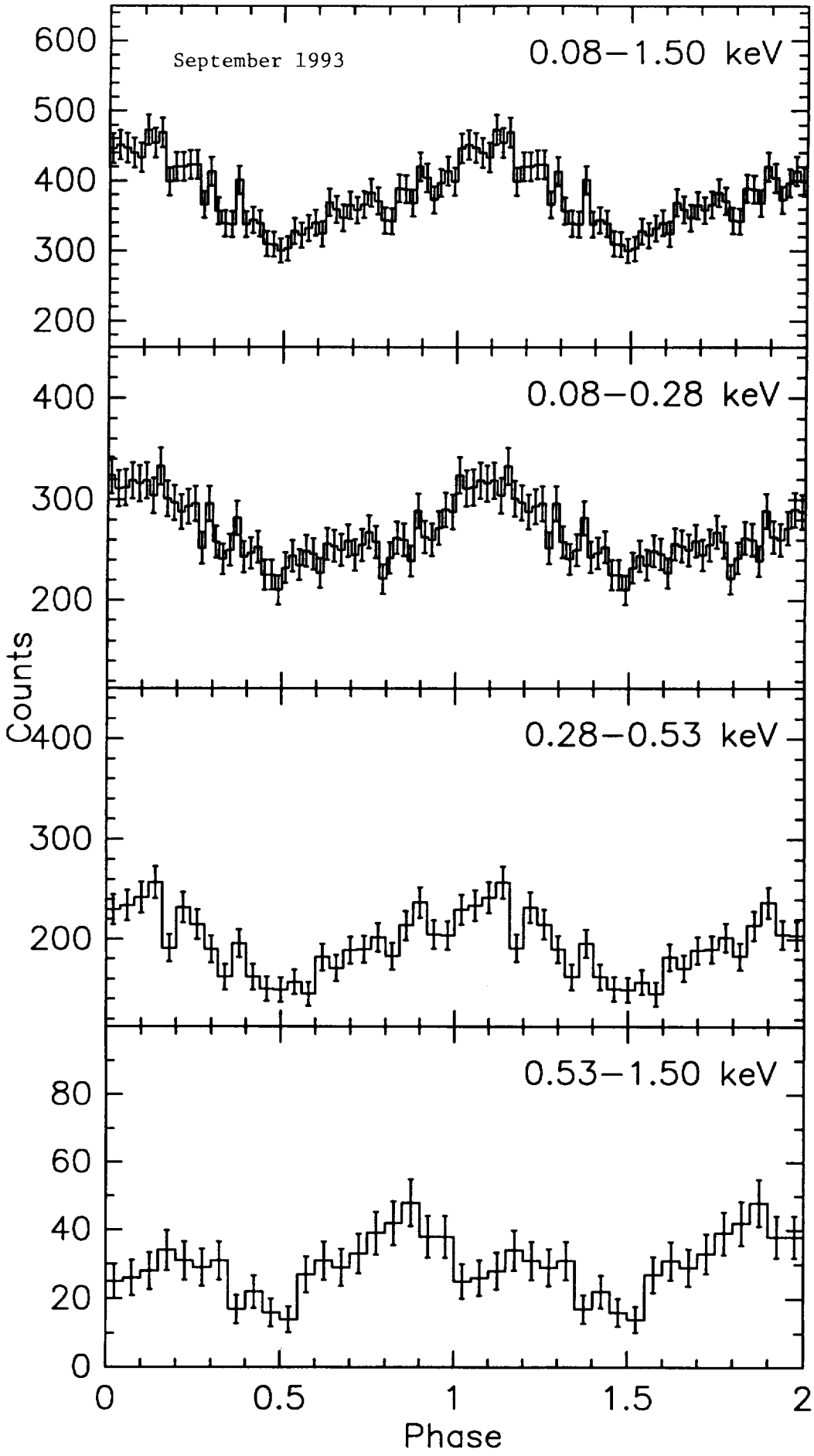
September 1993
0.08–1.50 keV
0.08–0.28 keV
0.28–0.53 keV
0.53–1.50 keV
Counts
Phase
600
500
400
300
200
400
300
200
400
300
200
80
60
40
20
0
0
0.5
1
1.5
2

Fig. 3

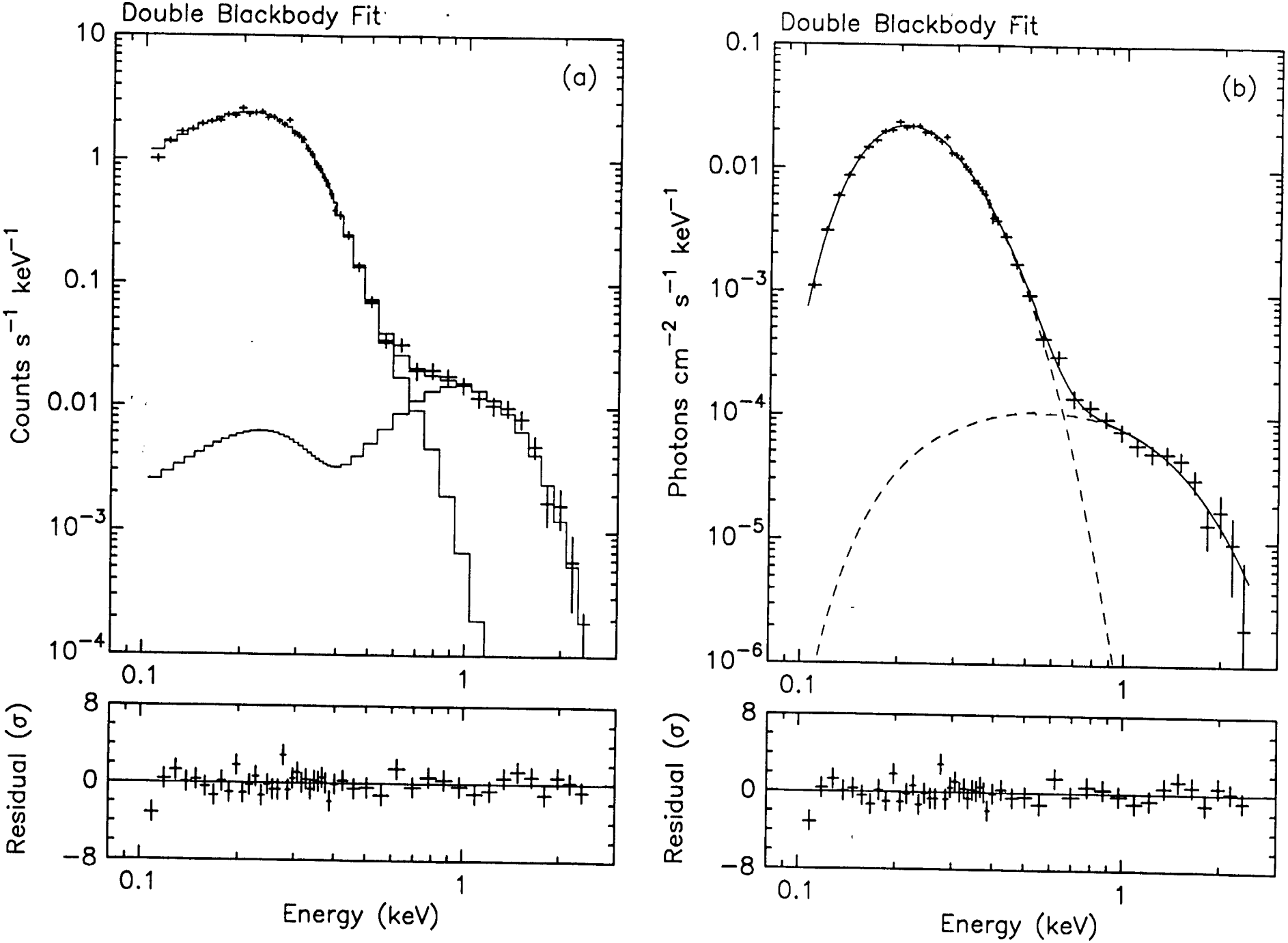
Double Blackbody Fit
(a)
Counts s^{-1} keV^{-1}
Residual (σ)
Energy (keV)
Double Blackbody Fit
(b)
Photons cm^{-2} s^{-1} keV^{-1}
Residual (σ)
Energy (keV)

Fig. 4

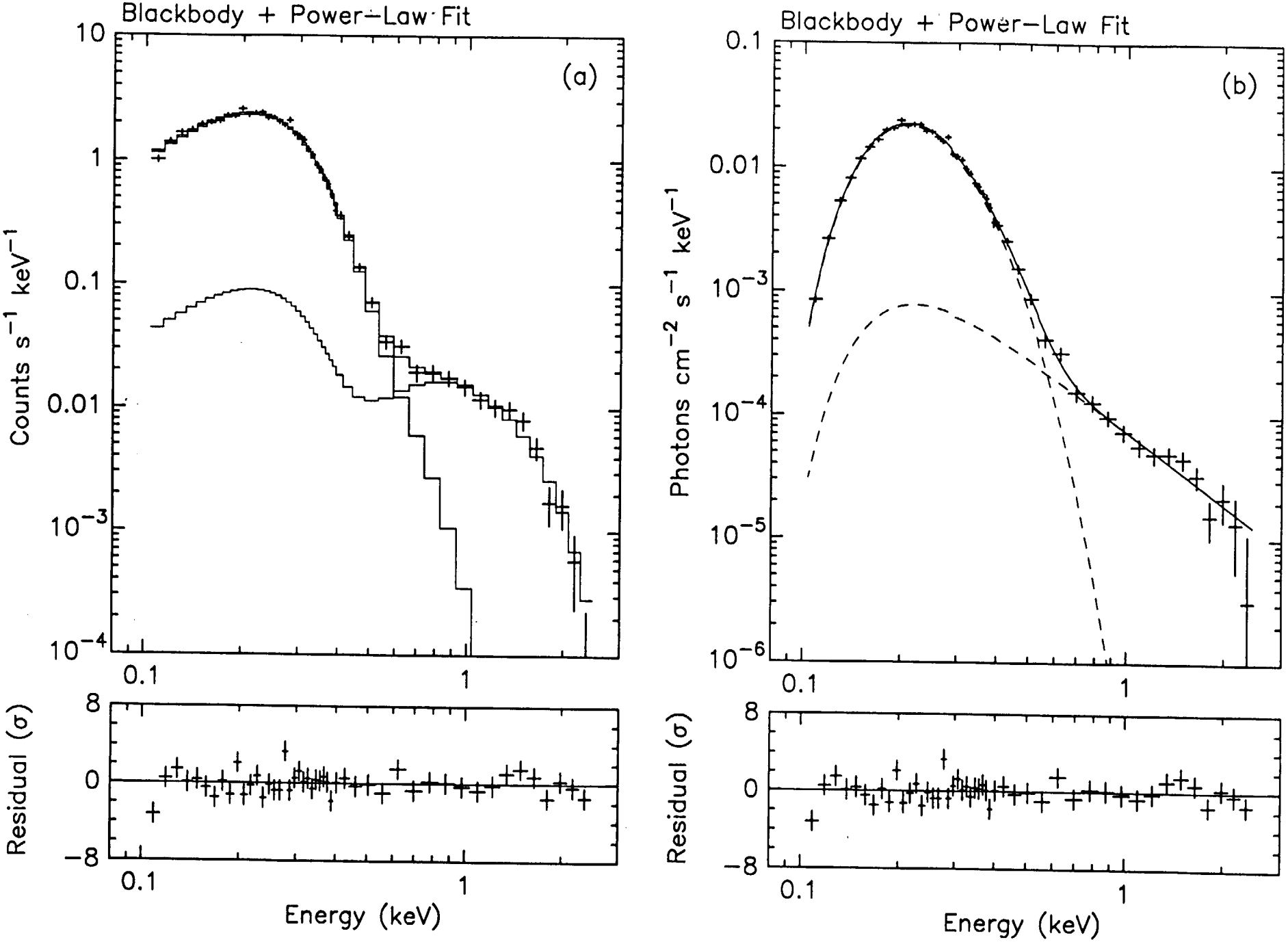
Blackbody + Power−Law Fit
(a)
Counts s^{-1} keV^{-1}
Residual (σ)
Energy (keV)
Blackbody + Power−Law Fit
(b)
Photons cm^{-2} s^{-1} keV^{-1}
Residual (σ)
Energy (keV)

Fig. 5

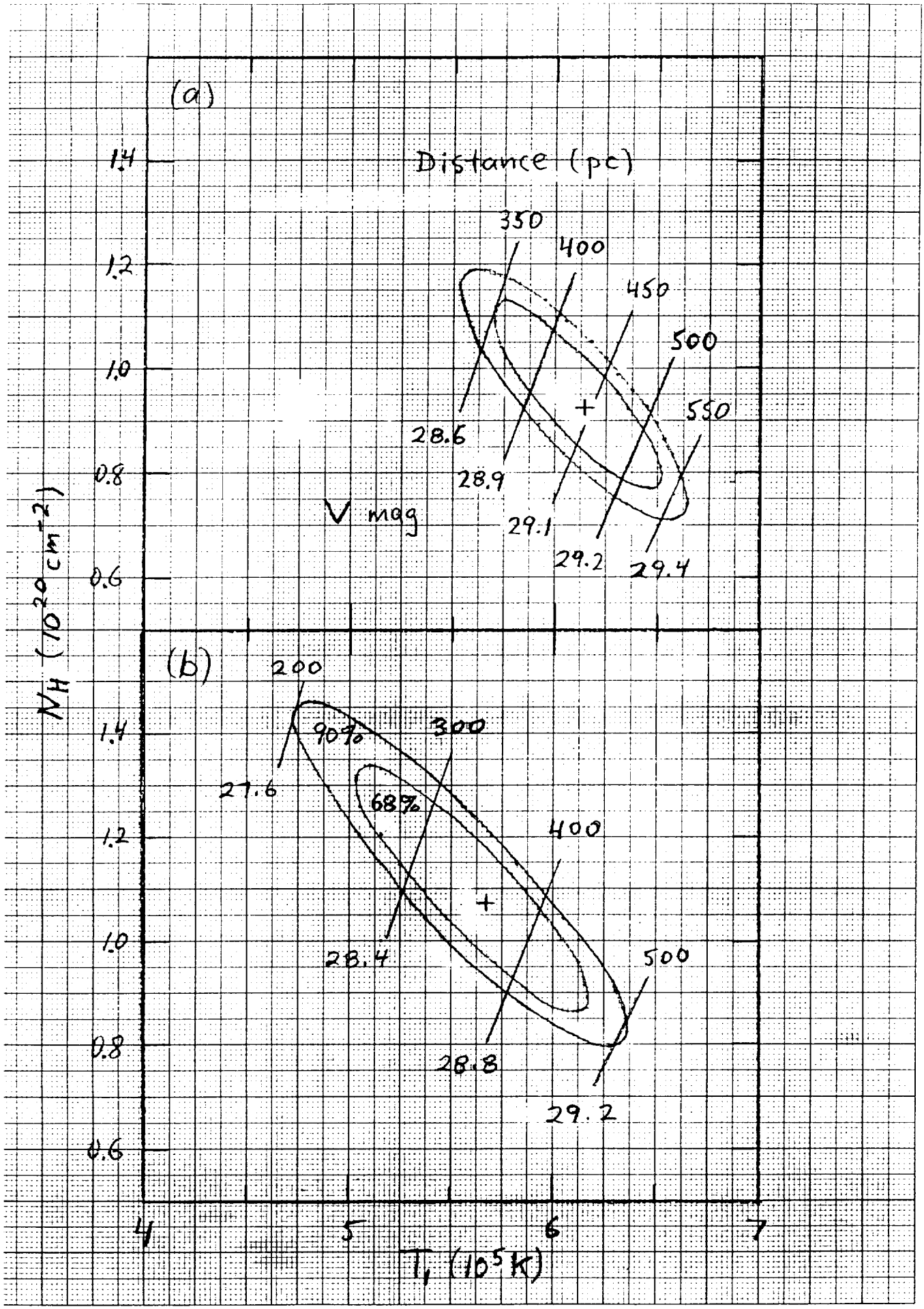
(a)
Distance (pc)
350
400
450
500
550
28.6
28.9
29.1
29.2
29.4
V mag
(b)
200
300
400
500
90%
68%
27.6
28.4
28.8
29.2
N_H (10^{20} cm^{-2})
1.4
1.2
1.0
0.8
0.6
4
5
6
7
T_1 (10^5 K)

Fig. 6

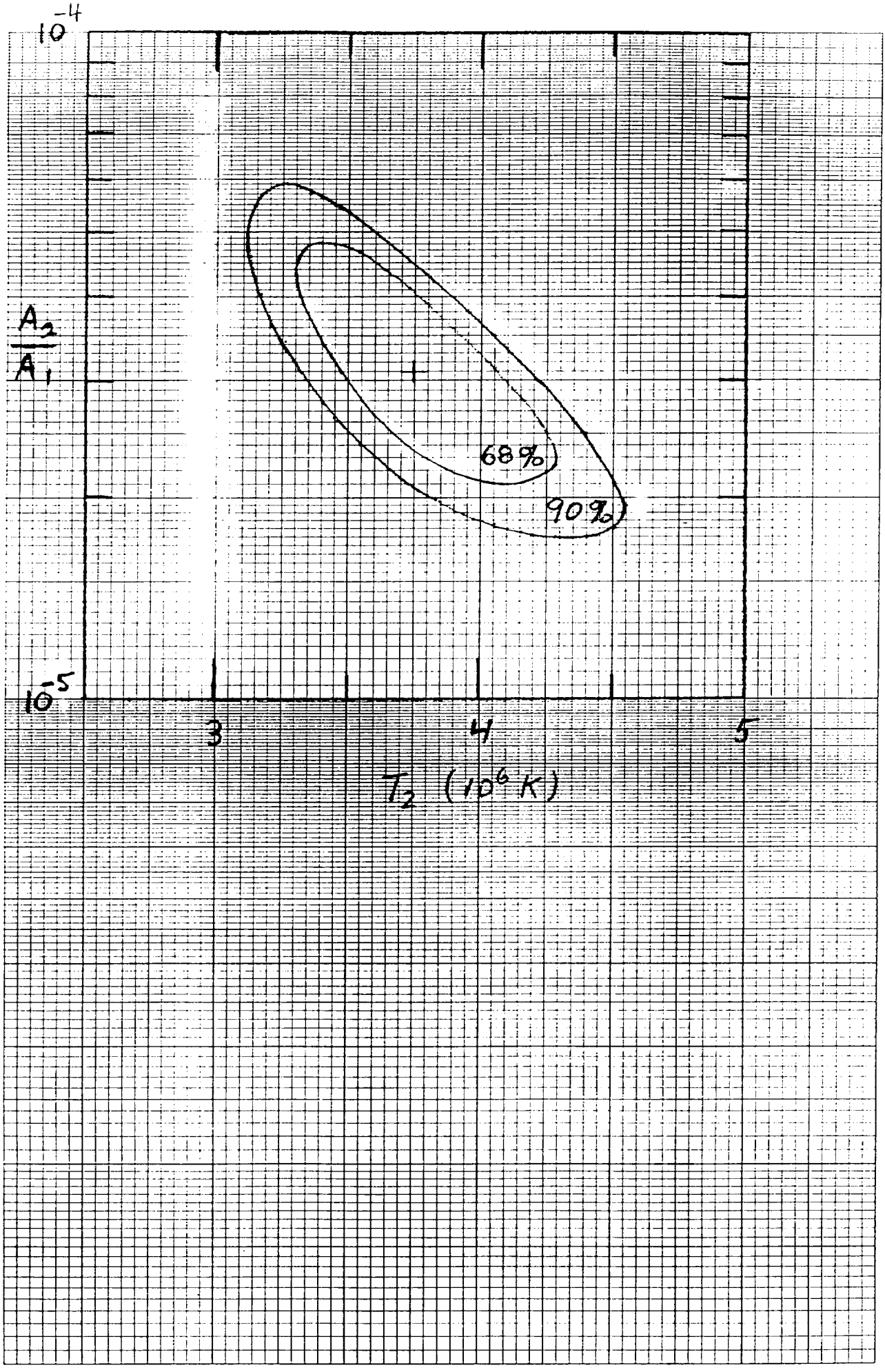

Fig. 7

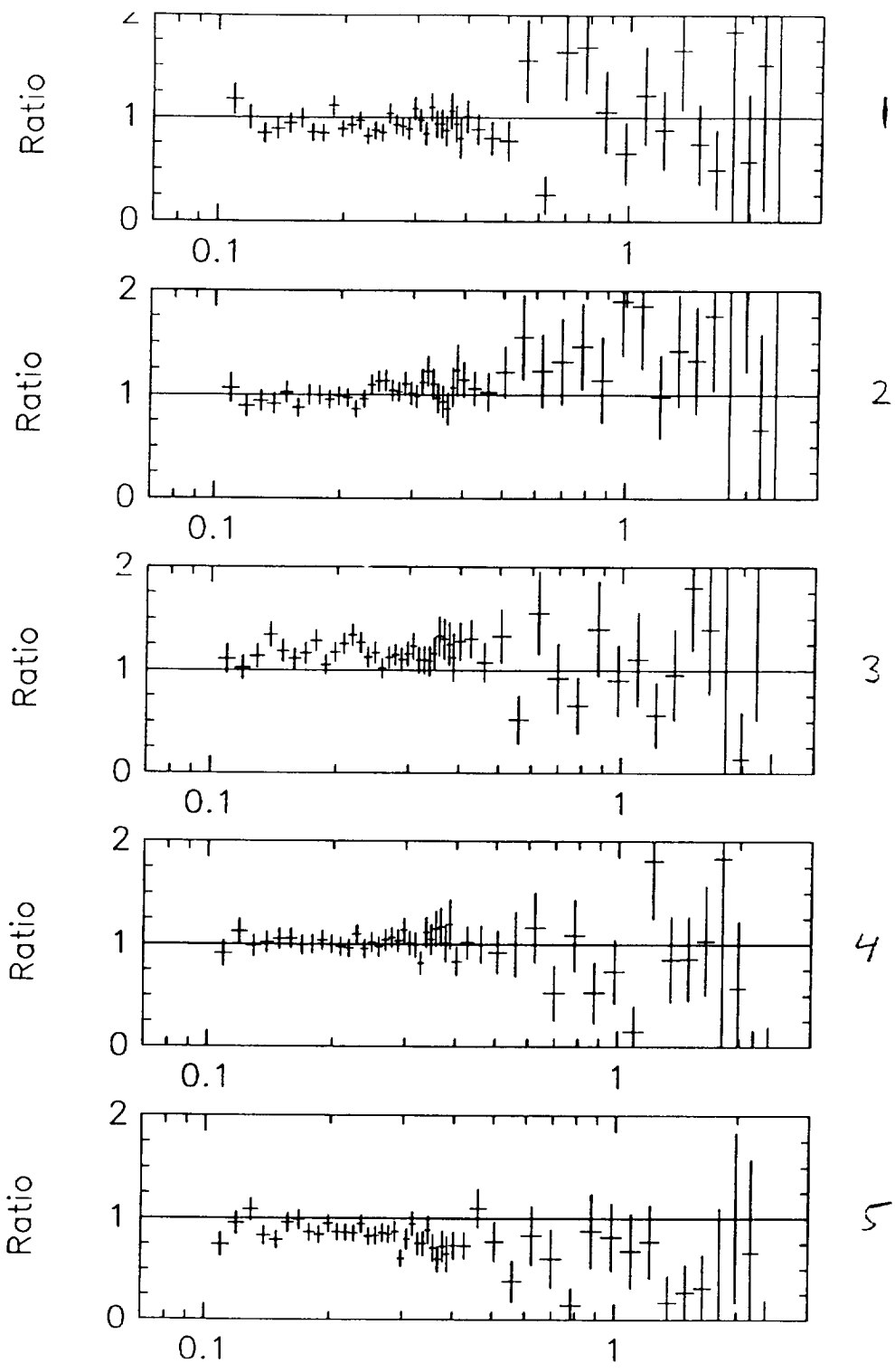

Fig. 9

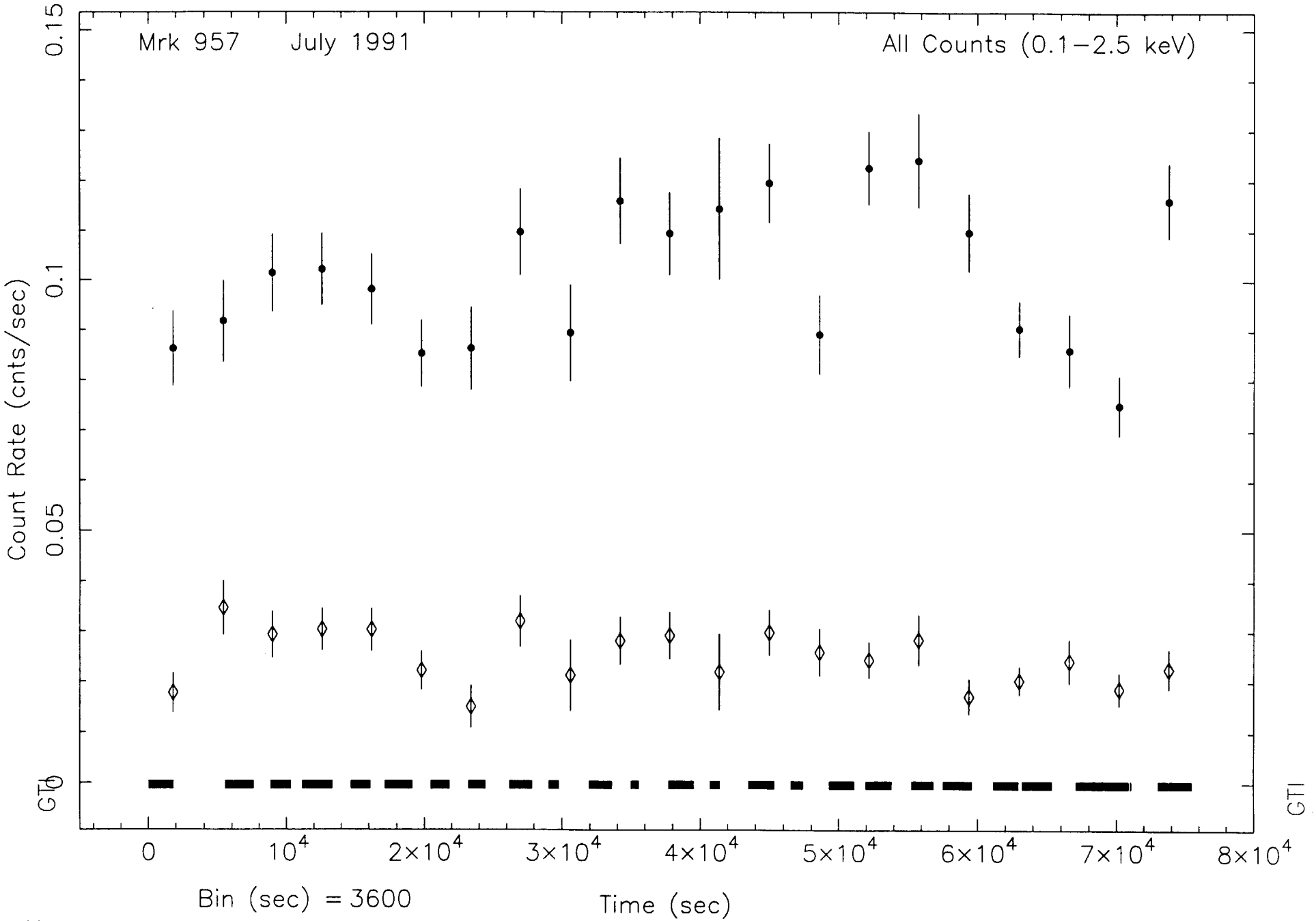
Mrk 957 July 1991
All Counts (0.1−2.5 keV)
Count Rate (cnts/sec)
0.15
0.1
0.05
0
GTI
GTI
0
10^4
2×10^4
3×10^4
4×10^4
5×10^4
6×10^4
7×10^4
8×10^4
Bin (sec) = 3600
Time (sec)

Fig. 10

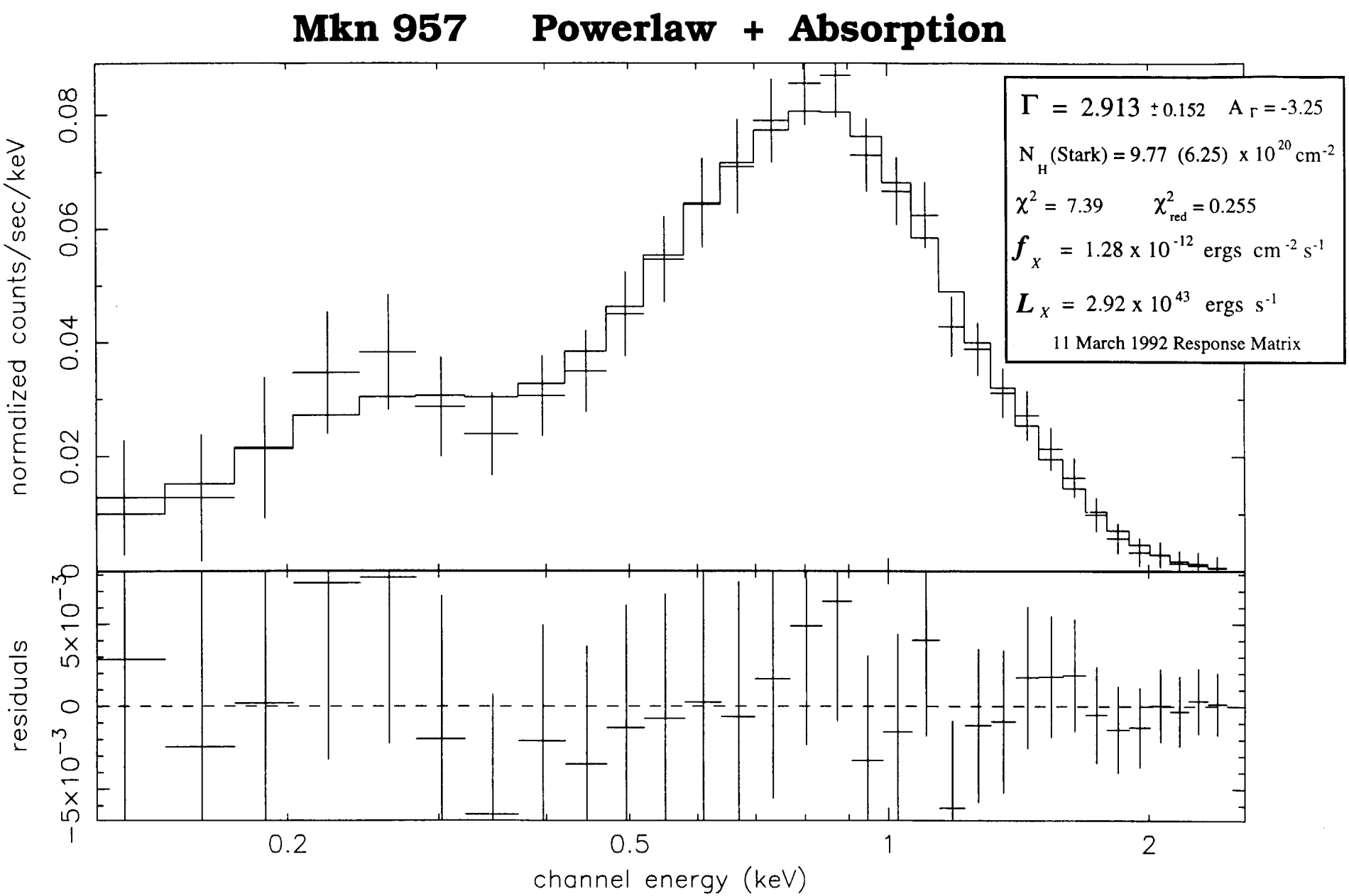
Mkn 957 Powerlaw + Absorption
Γ = 2.913 ± 0.152 A Γ = -3.25
N H (Stark) = 9.77 (6.25) x 10^20 cm^-2
χ^2 = 7.39 χ^2 red = 0.255
f X = 1.28 x 10^-12 ergs cm^-2 s^-1
L X = 2.92 x 10^43 ergs s^-1
11 March 1992 Response Matrix
normalized counts/sec/keV
0.02
0.04
0.06
0.08
residuals
-5x10^-3
0
5x10^-3
0.2
0.5
1
2
channel energy (keV)

Fig. 11

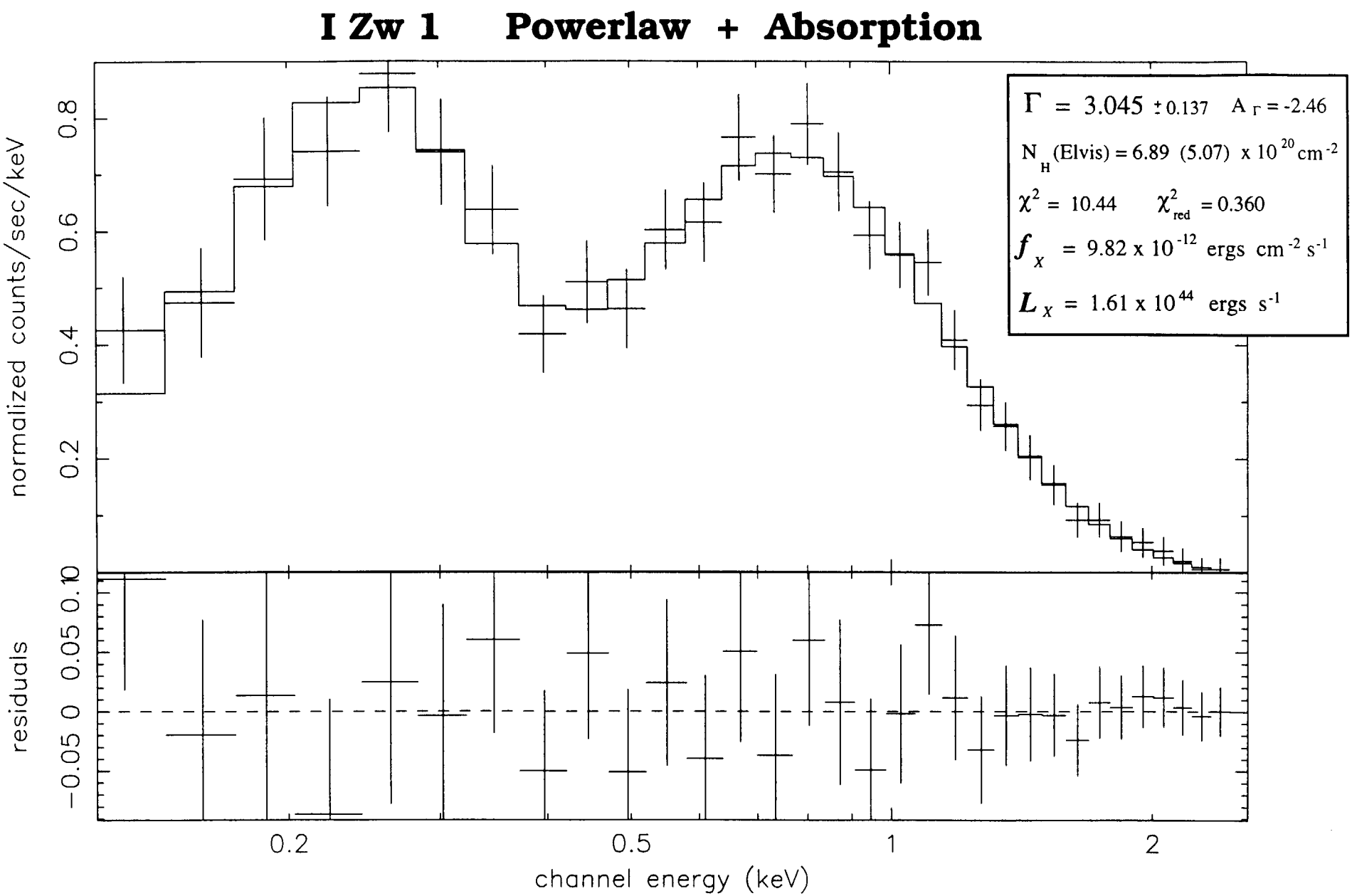
I Zw 1 Powerlaw + Absorption
Γ = 3.045 ± 0.137 A Γ = -2.46
N H (Elvis) = 6.89 (5.07) x 10 20 cm -2
χ 2 = 10.44 χ 2 red = 0.360
f X = 9.82 x 10 -12 ergs cm -2 s -1
L X = 1.61 x 10 44 ergs s -1
normalized counts/sec/keV
0.2
0.4
0.6
0.8
residuals
−0.05
0
0.05
0.10
0.2
0.5
1
2
channel energy (keV)

Fig. 12

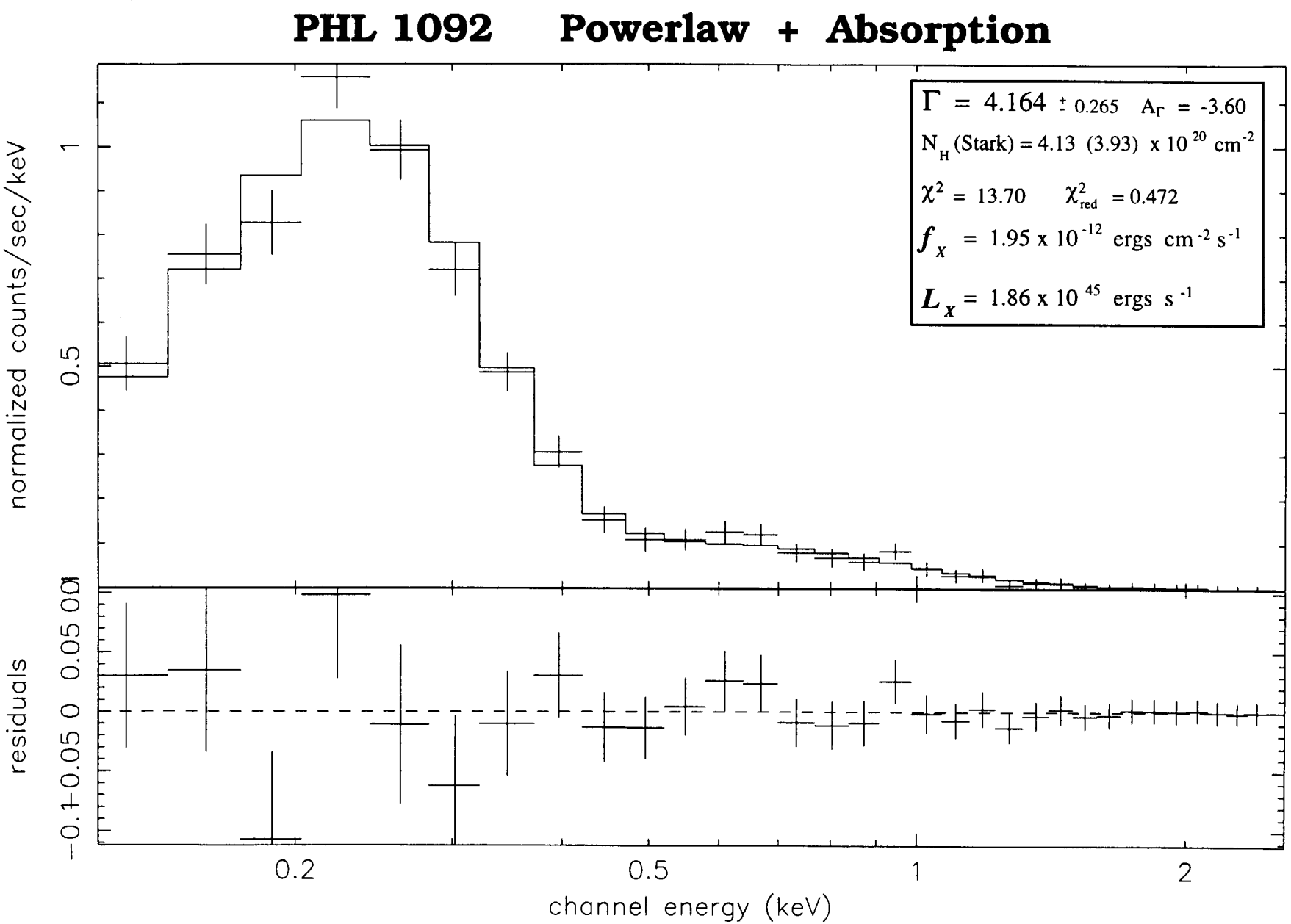
PHL 1092 Powerlaw + Absorption
Γ = 4.164 ± 0.265 AΓ = -3.60
N_H (Stark) = 4.13 (3.93) x 10^20 cm^-2
χ^2 = 13.70 χ^2_red = 0.472
f_X = 1.95 x 10^-12 ergs cm^-2 s^-1
L_X = 1.86 x 10^45 ergs s^-1
normalized counts/sec/keV
residuals
channel energy (keV)
0.2
0.5
1
2

Fig. 13

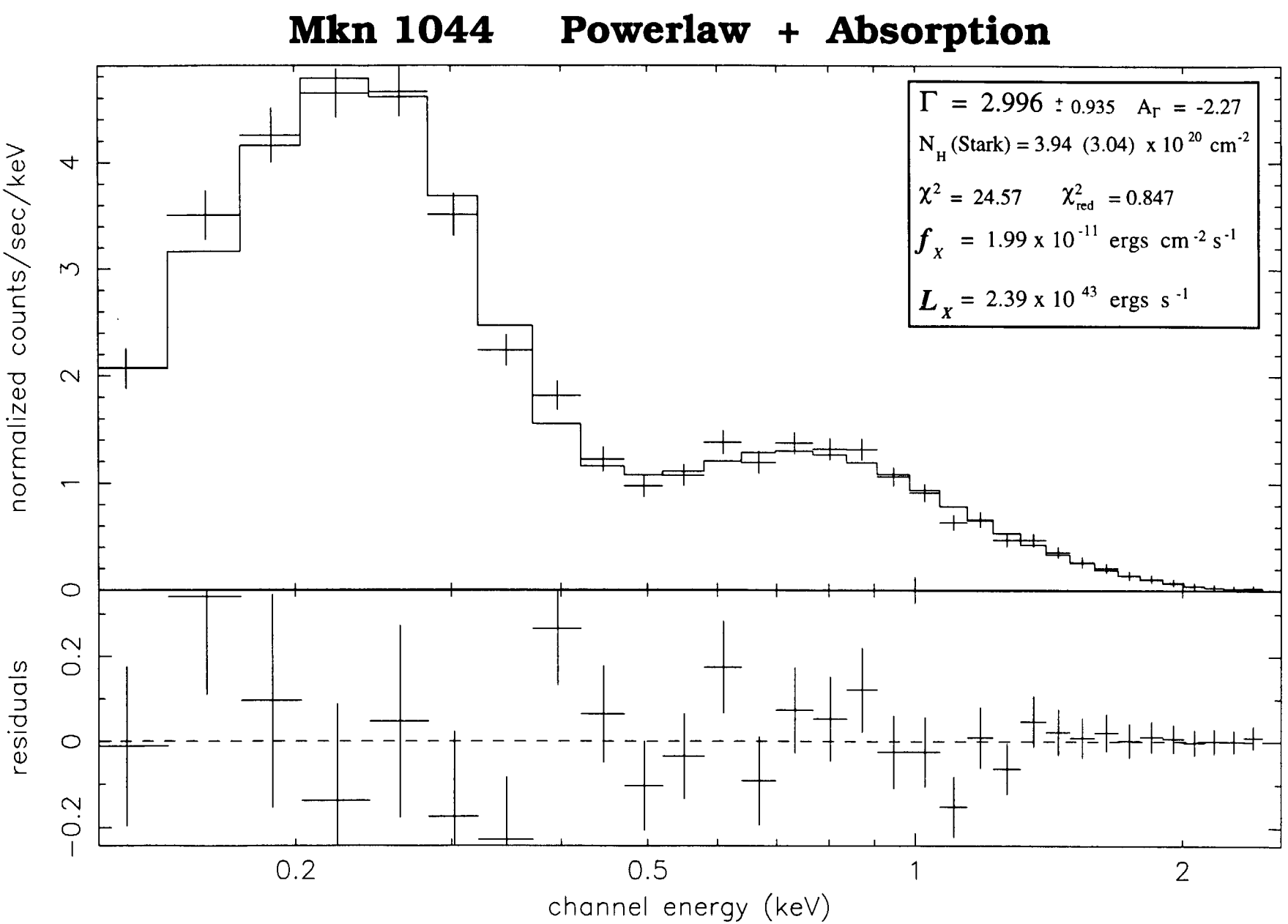
Mkn 1044 Powerlaw + Absorption
Γ = 2.996 ± 0.935 A_Γ = -2.27
N_H (Stark) = 3.94 (3.04) x 10^20 cm^-2
χ^2 = 24.57 χ^2_red = 0.847
f_X = 1.99 x 10^-11 ergs cm^-2 s^-1
L_X = 2.39 x 10^43 ergs s^-1
normalized counts/sec/keV
residuals
channel energy (keV)
0.2
0.5
1
2

Fig. 14

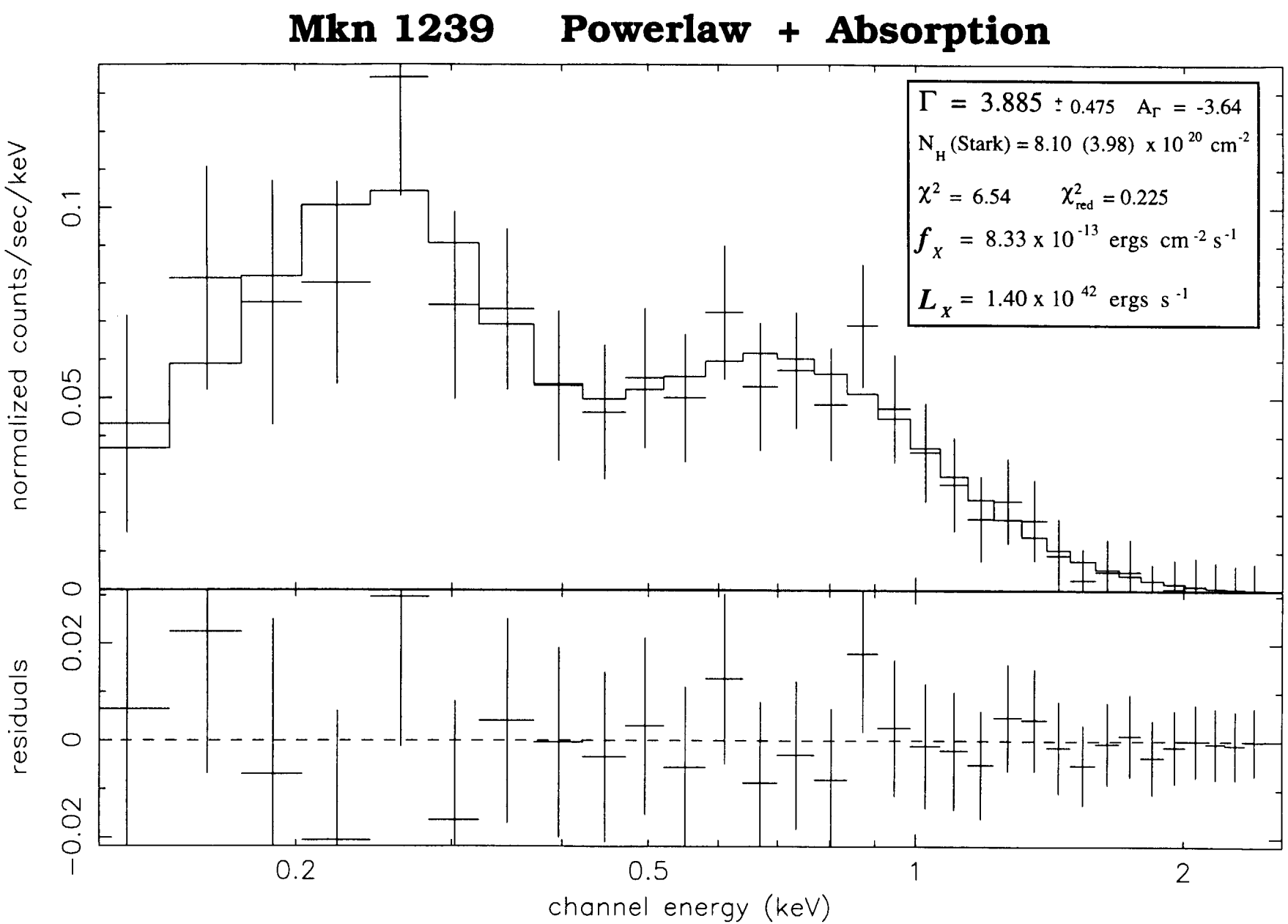
Mkn 1239 Powerlaw + Absorption
Γ = 3.885 ± 0.475 A_Γ = -3.64
N_H (Stark) = 8.10 (3.98) x 10^20 cm^-2
χ^2 = 6.54 χ^2_red = 0.225
f_X = 8.33 x 10^-13 ergs cm^-2 s^-1
L_X = 1.40 x 10^42 ergs s^-1
normalized counts/sec/keV
0.1
0.05
residuals
0.02
0
-0.02
0.2
0.5
1
2
channel energy (keV)

Fig. 15

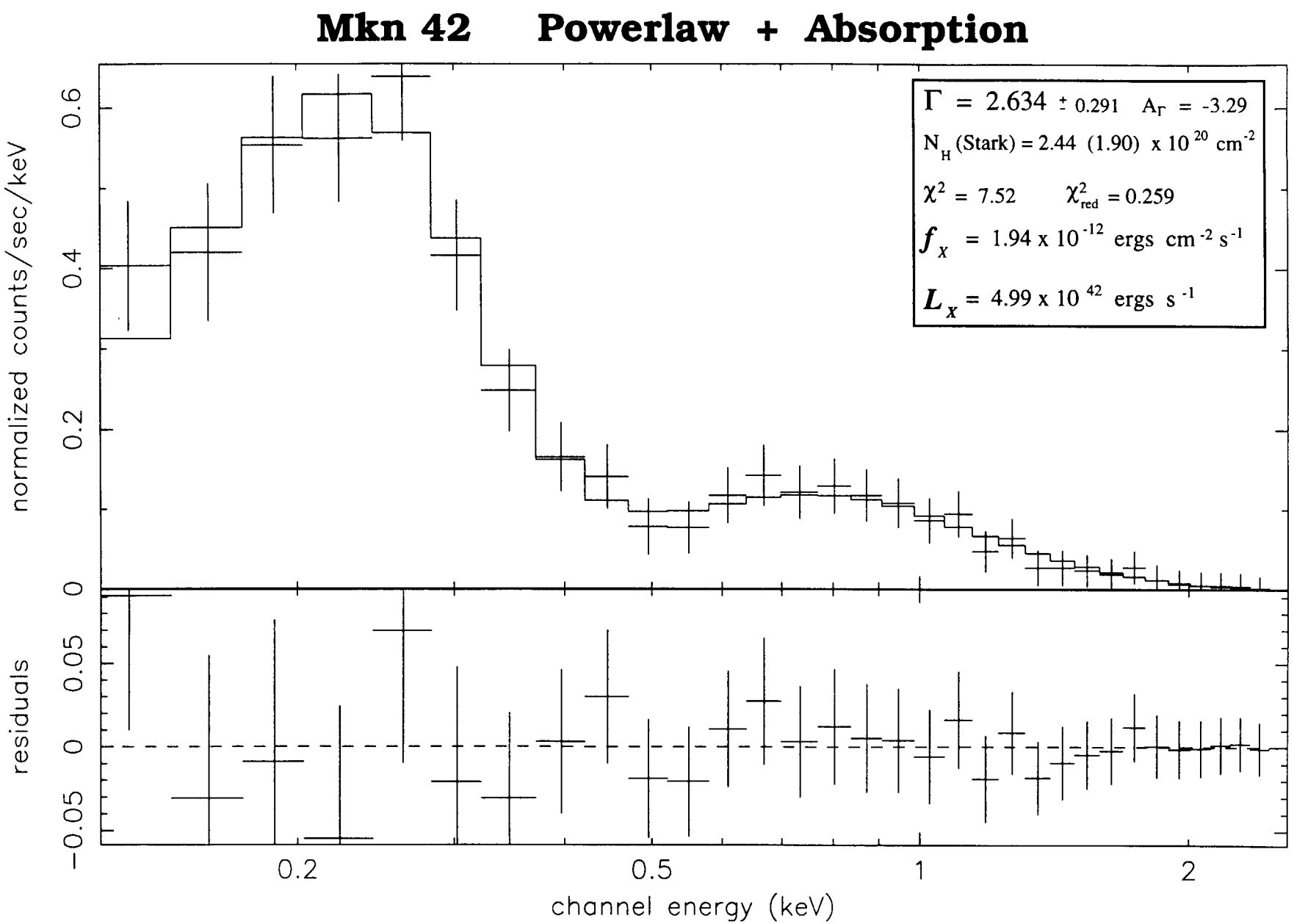
Mkn 42 Powerlaw + Absorption
Γ = 2.634 ± 0.291 A_Γ = -3.29
N_H (Stark) = 2.44 (1.90) x 10^20 cm^-2
χ^2 = 7.52 χ^2_red = 0.259
f_X = 1.94 x 10^-12 ergs cm^-2 s^-1
L_X = 4.99 x 10^42 ergs s^-1
normalized counts/sec/keV
0.6
0.4
0.2
0
residuals
0.05
0
−0.05
0.2
0.5
1
2
channel energy (keV)

Fig. 16

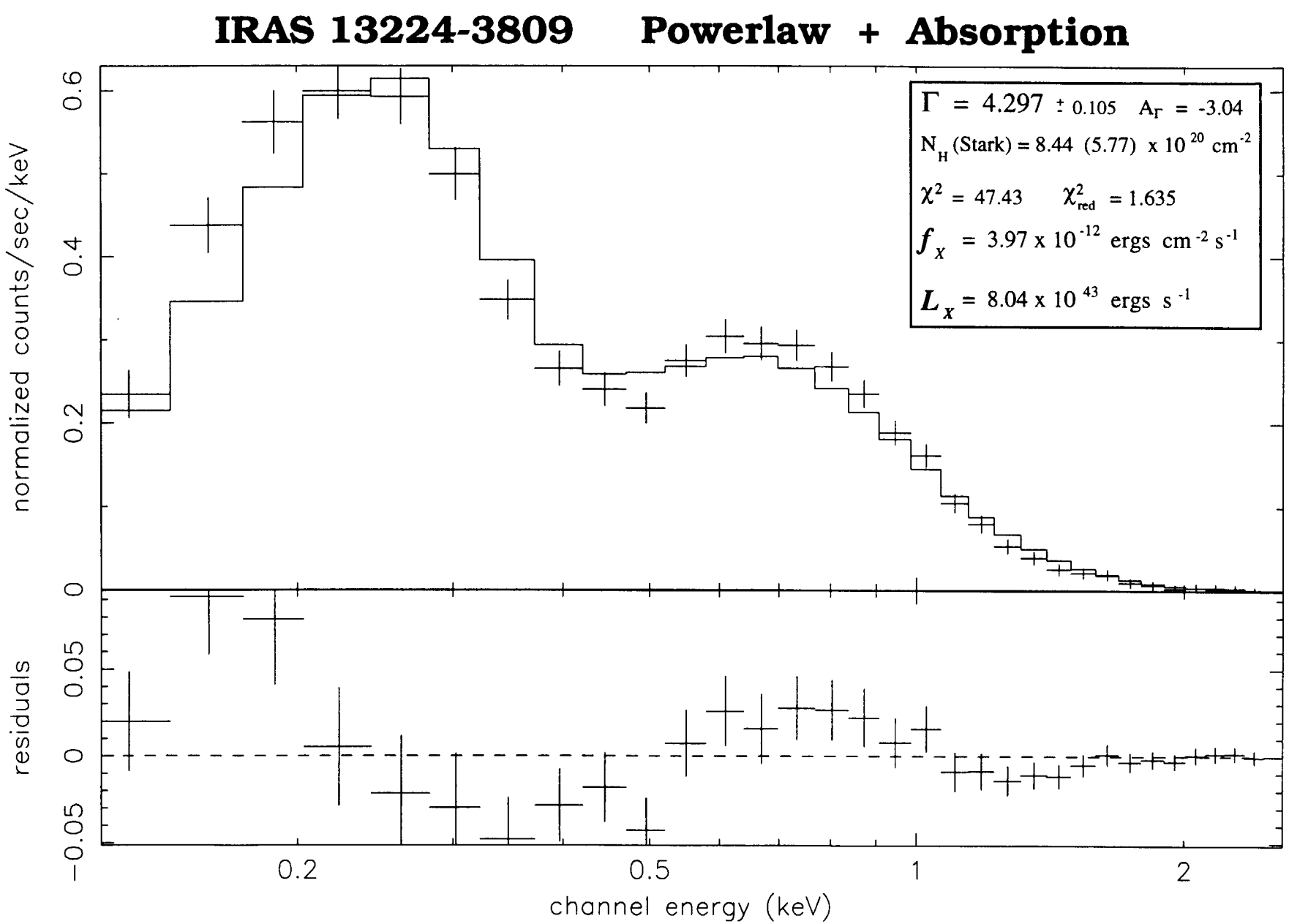
IRAS 13224-3809 Powerlaw + Absorption
Γ = 4.297 ± 0.105 A_Γ = -3.04
N_H (Stark) = 8.44 (5.77) x 10^20 cm^-2
χ^2 = 47.43 χ^2_red = 1.635
f_X = 3.97 x 10^-12 ergs cm^-2 s^-1
L_X = 8.04 x 10^43 ergs s^-1
normalized counts/sec/keV
0.6
0.4
0.2
0
residuals
0.05
0
−0.05
0.2
0.5
1
2
channel energy (keV)

Fig. 17

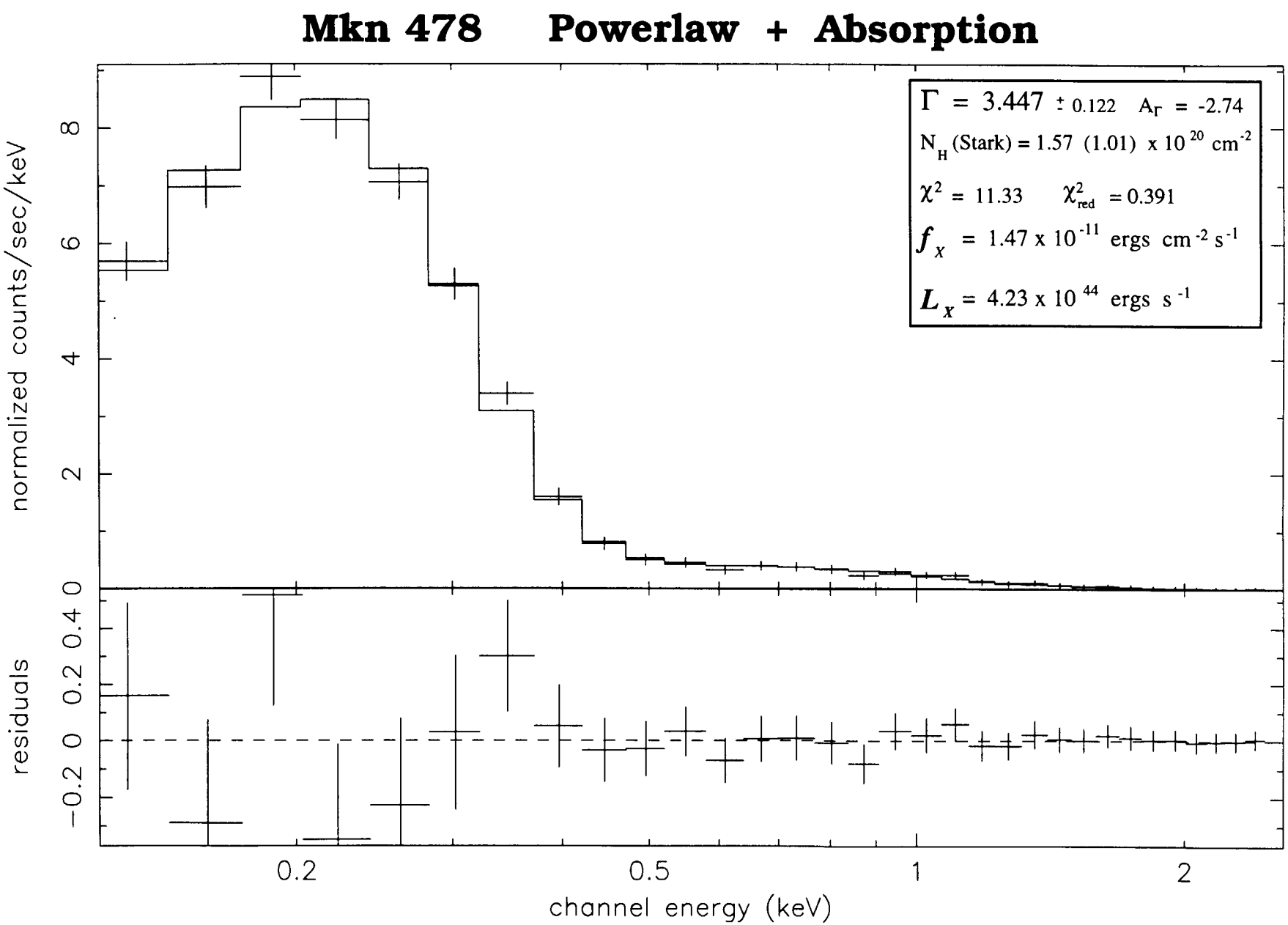
Mkn 478 Powerlaw + Absorption
Γ = 3.447 ± 0.122 AΓ = -2.74
N_H (Stark) = 1.57 (1.01) x 10^20 cm^-2
χ^2 = 11.33 χ^2_red = 0.391
f_X = 1.47 x 10^-11 ergs cm^-2 s^-1
L_X = 4.23 x 10^44 ergs s^-1
normalized counts/sec/keV
residuals
channel energy (keV)
0.2
0.5
1
2

Fig. 18

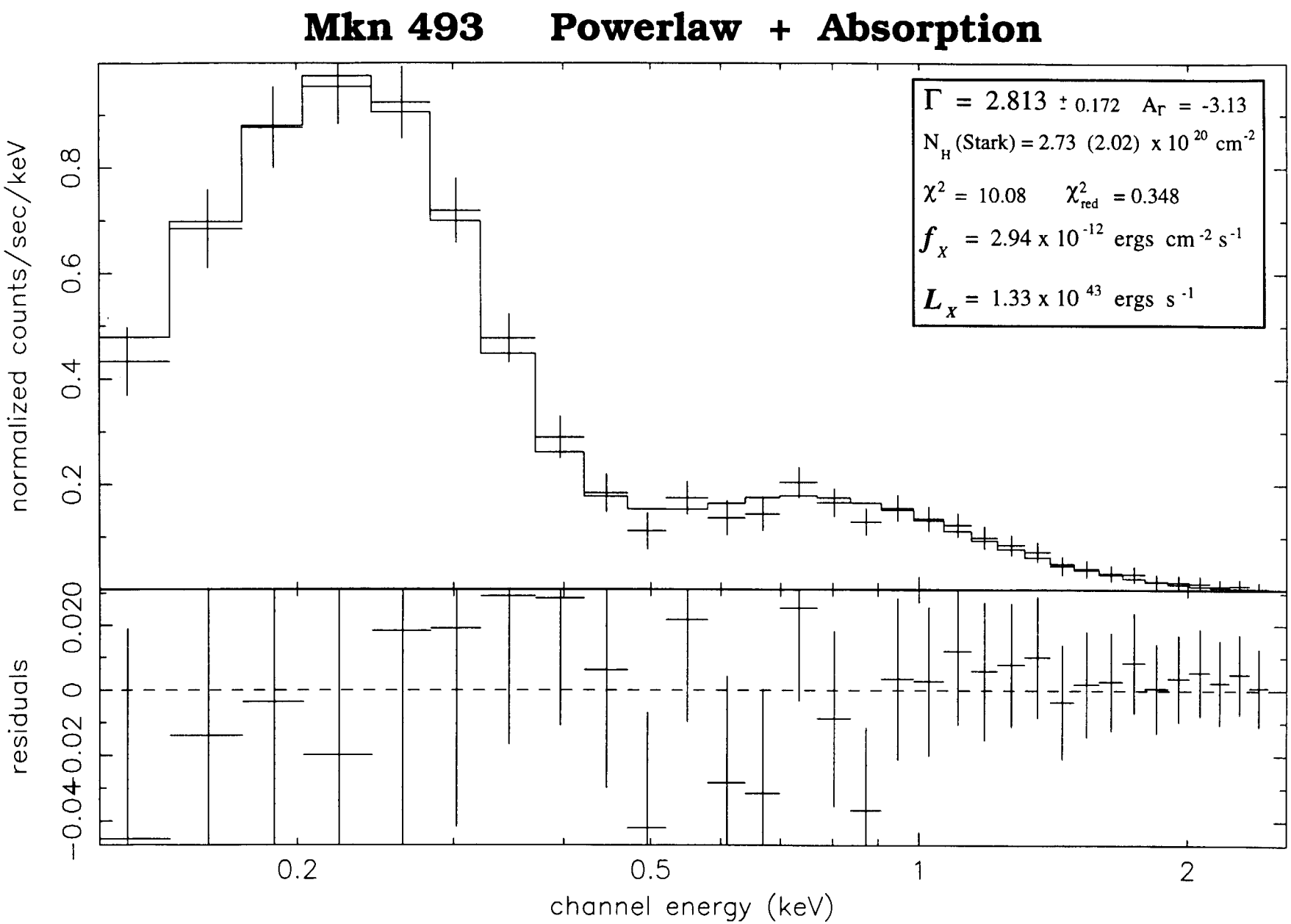
Mkn 493 Powerlaw + Absorption
Γ = 2.813 ± 0.172 A_Γ = -3.13
N_H (Stark) = 2.73 (2.02) x 10^20 cm^-2
χ^2 = 10.08 χ^2_red = 0.348
f_X = 2.94 x 10^-12 ergs cm^-2 s^-1
L_X = 1.33 x 10^43 ergs s^-1
normalized counts/sec/keV
0.2
0.4
0.6
0.8
residuals
−0.04
−0.02
0
0.020
0.2
0.5
1
2
channel energy (keV)

Fig. 19

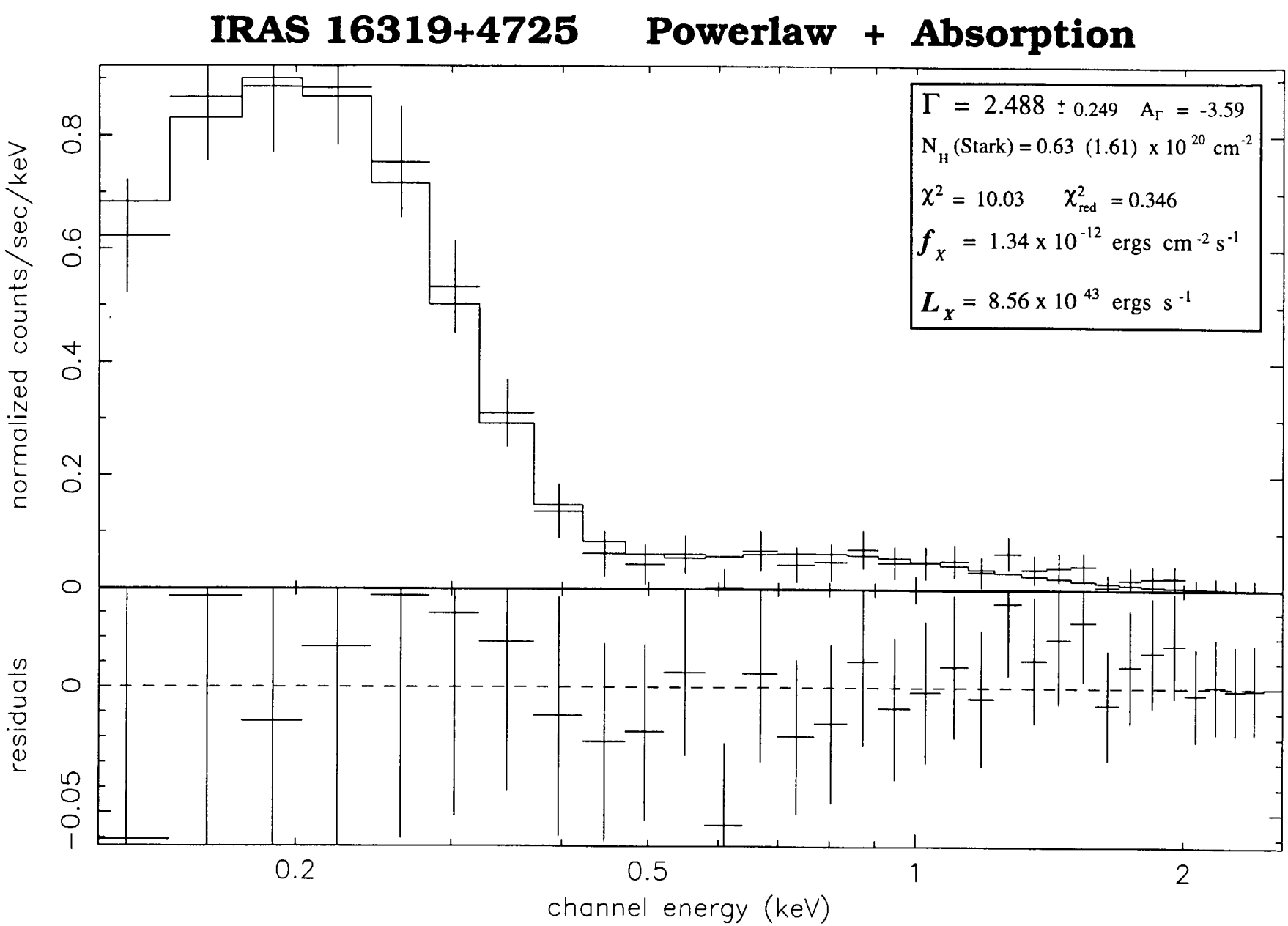
IRAS 16319+4725 Powerlaw + Absorption
Γ = 2.488 ± 0.249 A_Γ = -3.59
N_H (Stark) = 0.63 (1.61) x 10^20 cm^-2
χ^2 = 10.03 χ^2_red = 0.346
f_X = 1.34 x 10^-12 ergs cm^-2 s^-1
L_X = 8.56 x 10^43 ergs s^-1
normalized counts/sec/keV
residuals
channel energy (keV)
0.2
0.5
1
2
0.8
0.6
0.4
0.2
0
−0.05

Fig. 20

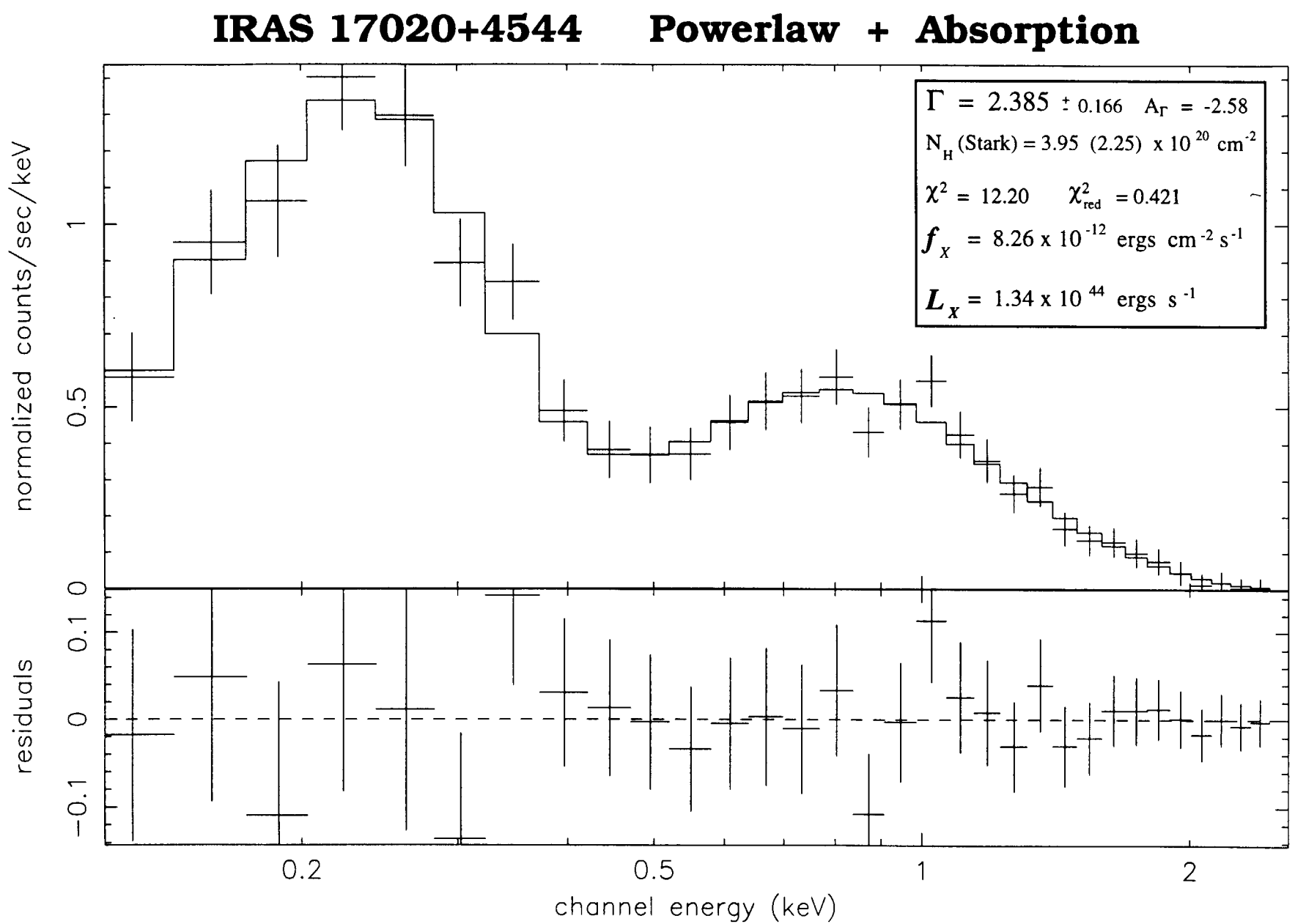
IRAS 17020+4544 Powerlaw + Absorption
Γ = 2.385 ± 0.166 AΓ = -2.58
N_H (Stark) = 3.95 (2.25) x 10^20 cm^-2
χ^2 = 12.20 χ^2_red = 0.421
f_X = 8.26 x 10^-12 ergs cm^-2 s^-1
L_X = 1.34 x 10^44 ergs s^-1
normalized counts/sec/keV
residuals
channel energy (keV)
0.2
0.5
1
2
0.5
1
0.1
0
−0.1

Fig. 21

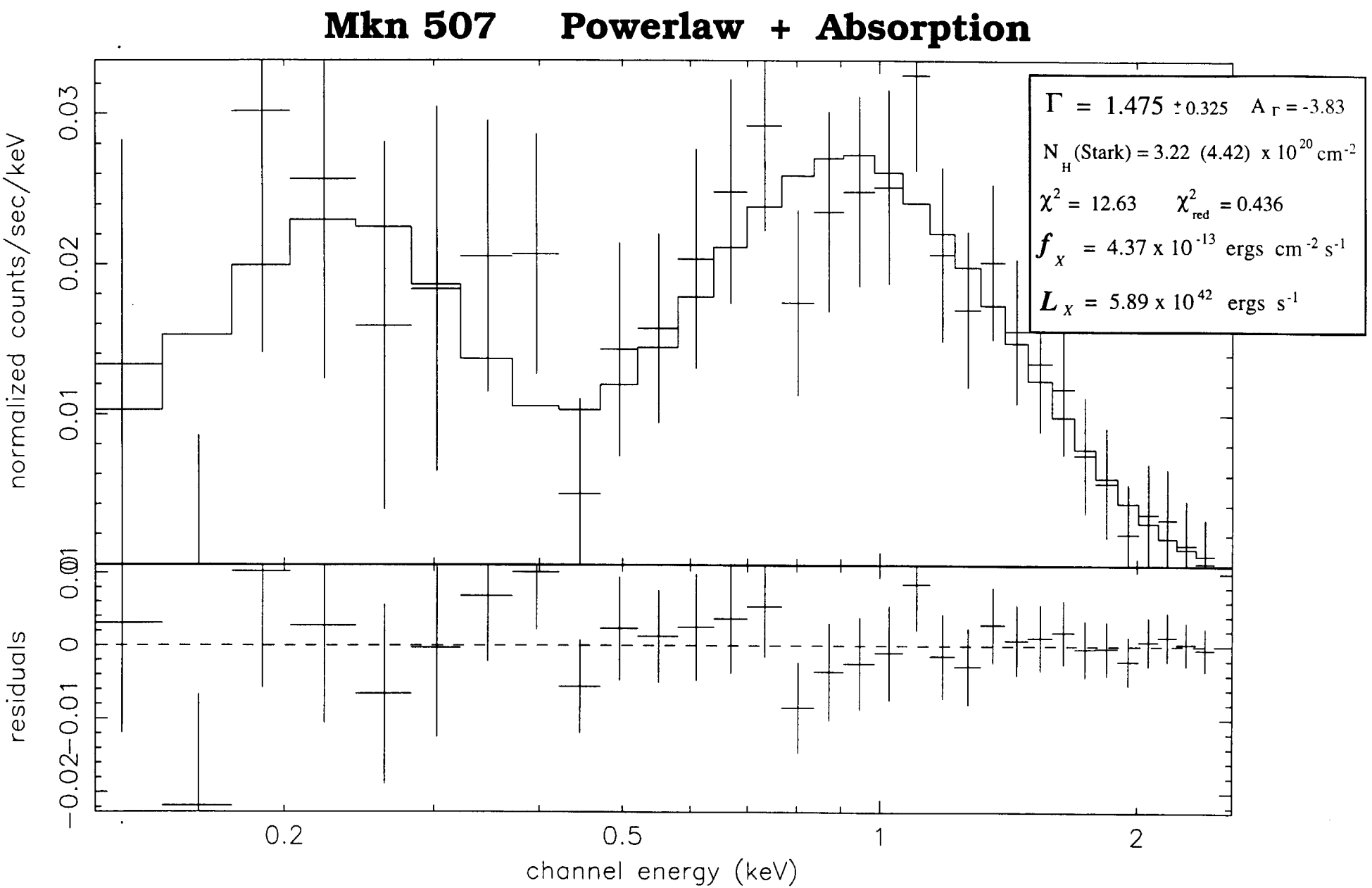
Mkn 507 Powerlaw + Absorption
Γ = 1.475 ± 0.325 A Γ = -3.83
N H (Stark) = 3.22 (4.42) x 10^20 cm^-2
χ^2 = 12.63 χ^2 red = 0.436
f X = 4.37 x 10^-13 ergs cm^-2 s^-1
L X = 5.89 x 10^42 ergs s^-1
normalized counts/sec/keV
0.03
0.02
0.01
residuals
0.01
0
−0.01
−0.02
0.2
0.5
1
2
channel energy (keV)

Fig. 22

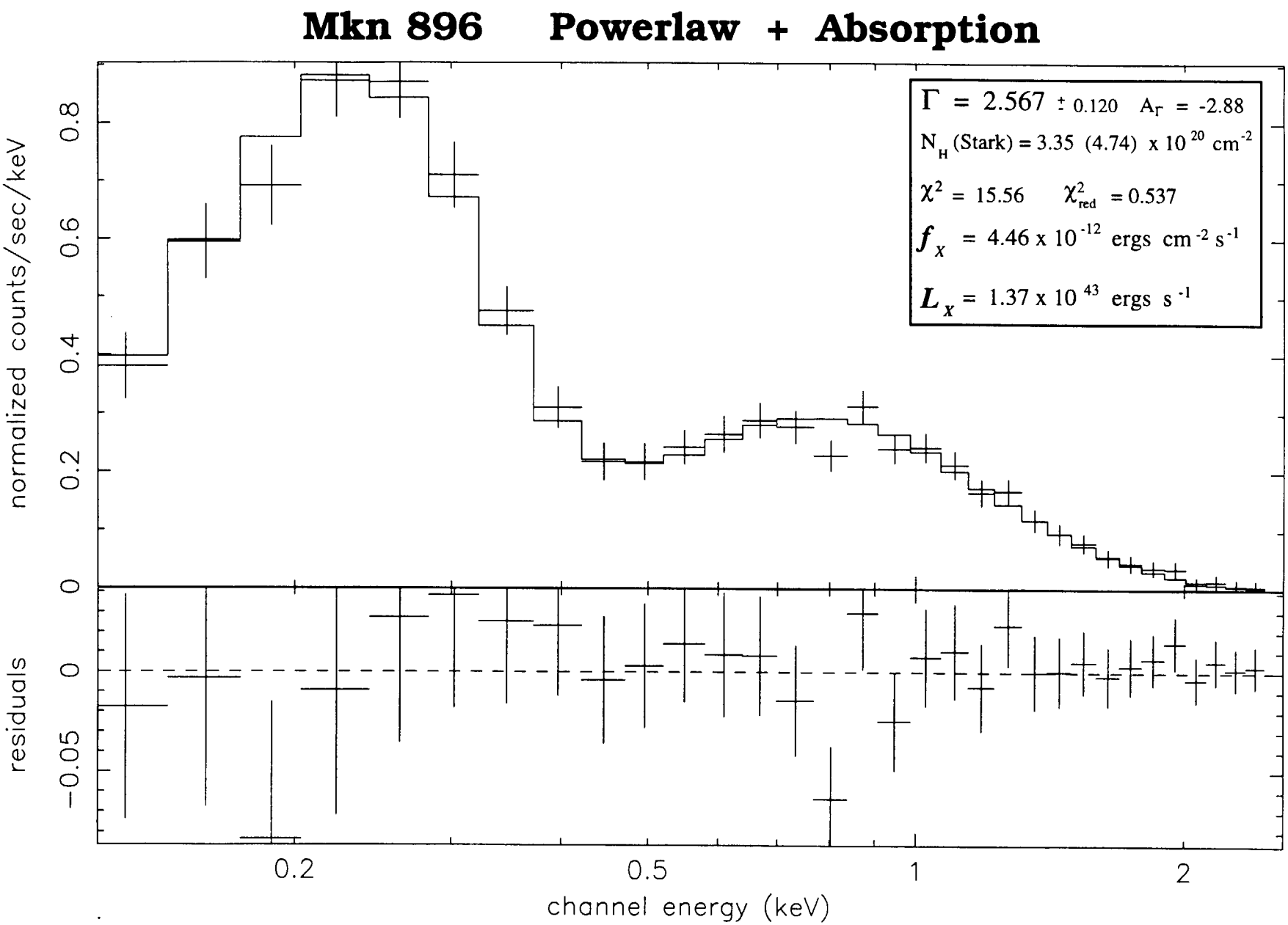
Mkn 896 Powerlaw + Absorption
Γ = 2.567 ± 0.120 A_Γ = -2.88
N_H (Stark) = 3.35 (4.74) x 10^20 cm^-2
χ^2 = 15.56 χ^2_red = 0.537
f_X = 4.46 x 10^-12 ergs cm^-2 s^-1
L_X = 1.37 x 10^43 ergs s^-1
normalized counts/sec/keV
residuals
channel energy (keV)
0.2
0.5
1
2
0.8
0.6
0.4
0.2
0
0
−0.05

Fig. 23

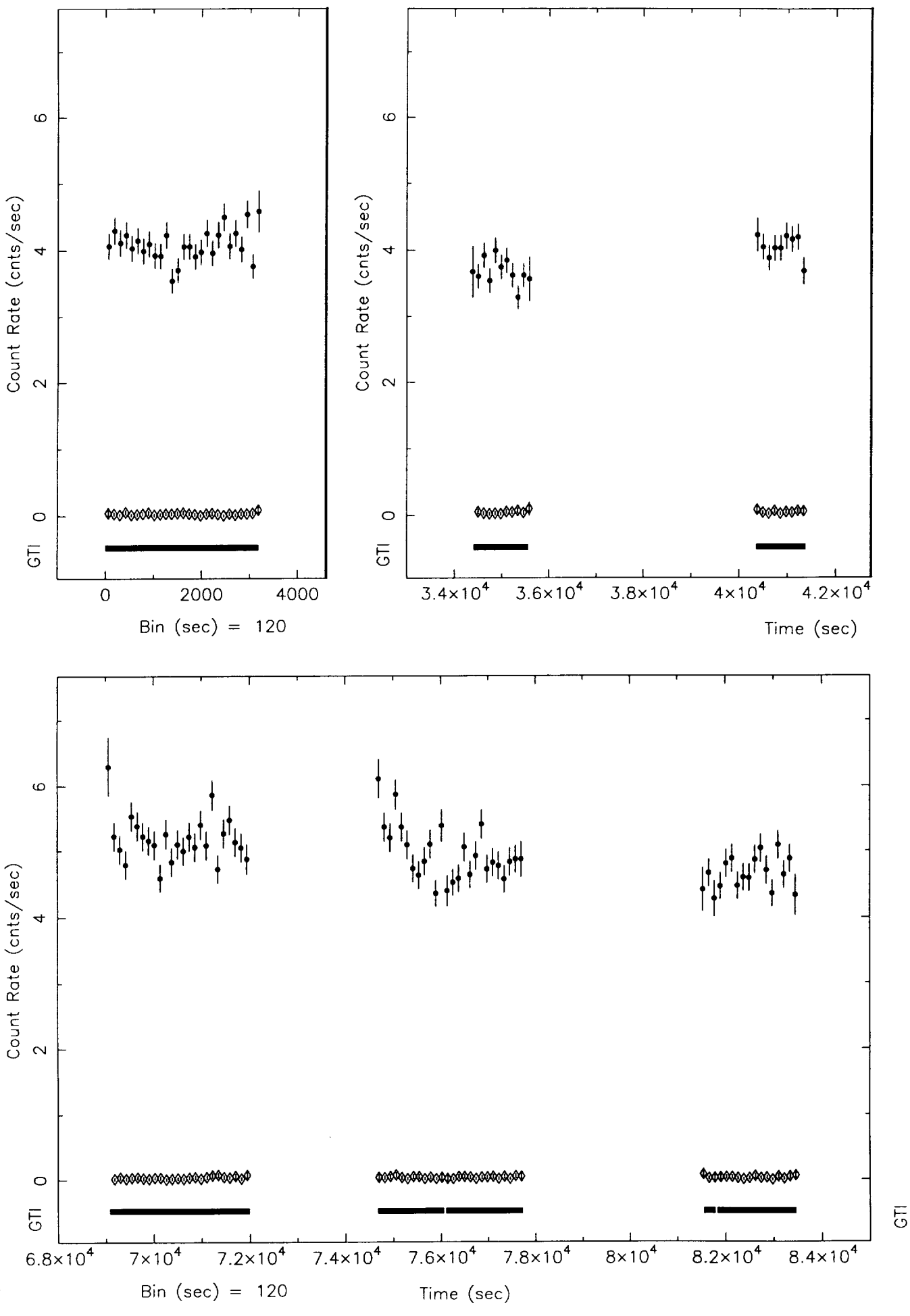
NGC 3516 October 1992 Lightcurve
All Counts (0.1 - 2.5 keV)
Count Rate (cnts/sec)
GTI
Bin (sec) = 120
Time (sec)
0
2000
4000
3.4×10^4
3.6×10^4
3.8×10^4
4×10^4
4.2×10^4
6.8×10^4
7×10^4
7.2×10^4
7.4×10^4
7.6×10^4
7.8×10^4
8×10^4
8.2×10^4
8.4×10^4

Fig. 24

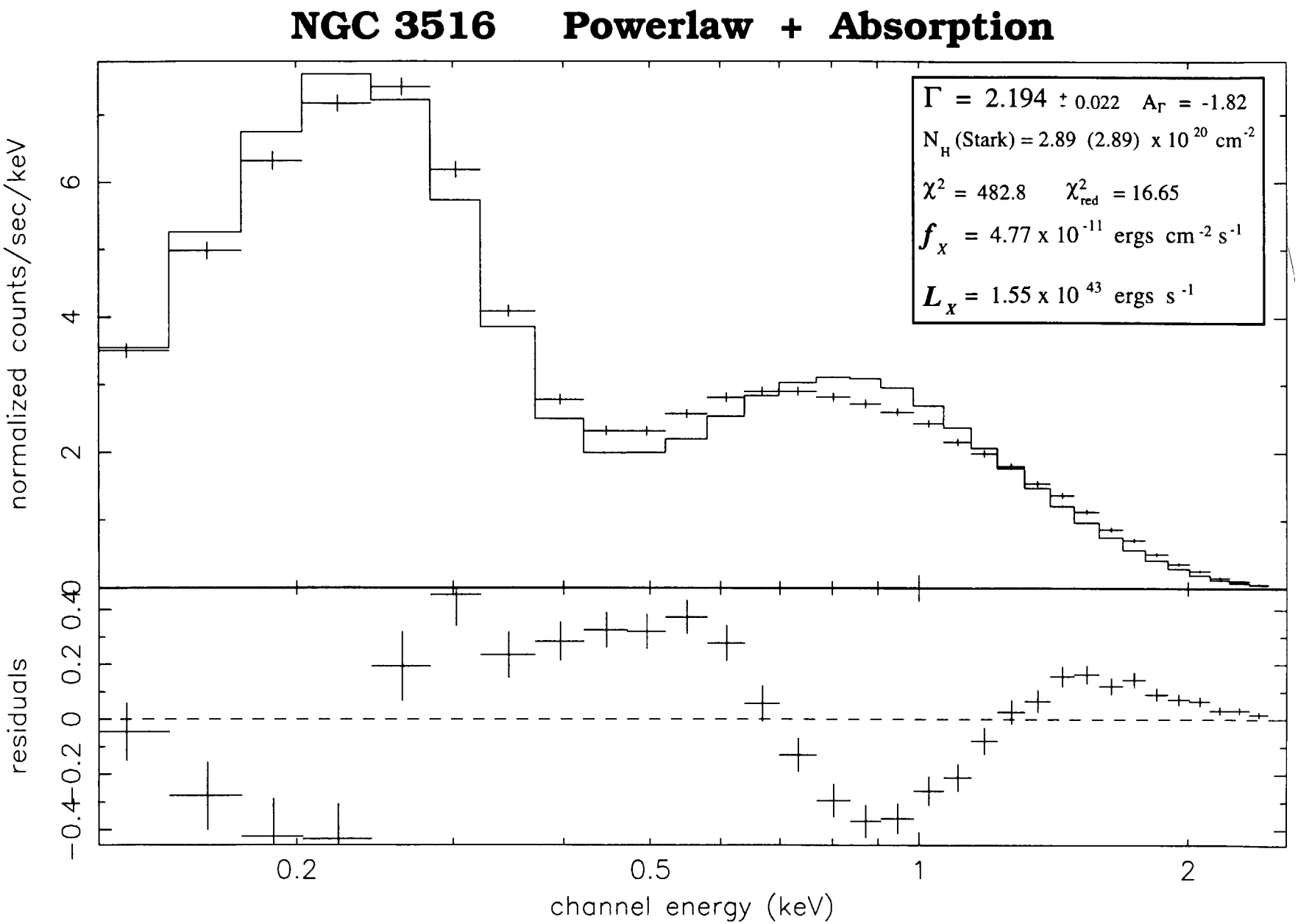
NGC 3516 Powerlaw + Absorption
Γ = 2.194 ± 0.022 A_Γ = -1.82
N_H (Stark) = 2.89 (2.89) x 10^20 cm^-2
χ^2 = 482.8 χ^2_red = 16.65
f_X = 4.77 x 10^-11 ergs cm^-2 s^-1
L_X = 1.55 x 10^43 ergs s^-1
normalized counts/sec/keV
residuals
channel energy (keV)
0.2
0.5
1
2

Fig. 25

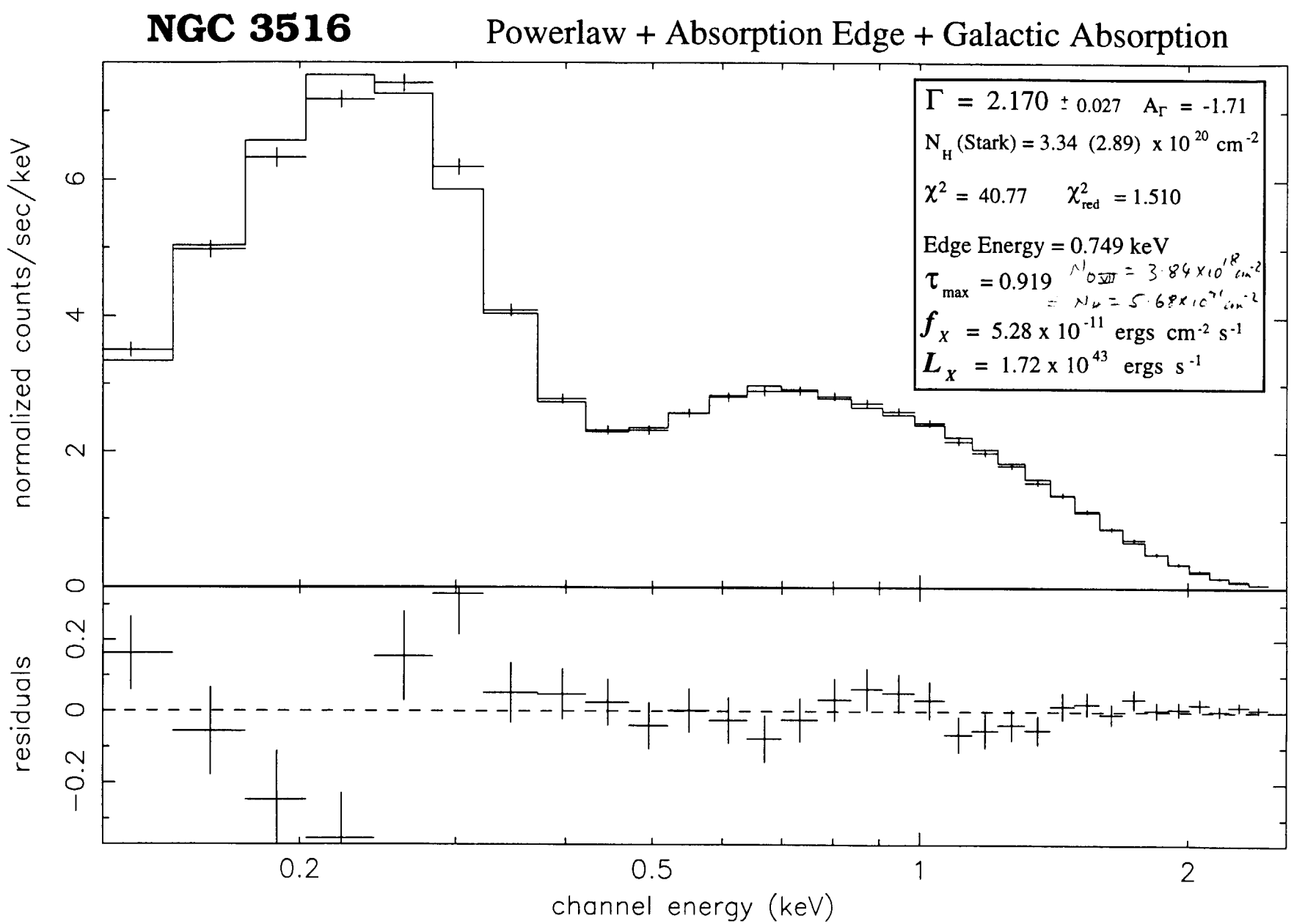
NGC 3516
Powerlaw + Absorption Edge + Galactic Absorption
Γ = 2.170 ± 0.027 A_Γ = -1.71
N_H (Stark) = 3.34 (2.89) x 10^20 cm^-2
χ^2 = 40.77 χ^2_red = 1.510
Edge Energy = 0.749 keV
τ_max = 0.919
f_X = 5.28 x 10^-11 ergs cm^-2 s^-1
L_X = 1.72 x 10^43 ergs s^-1
normalized counts/sec/keV
residuals
channel energy (keV)
0.2
0.5
1
2

Fig. 26

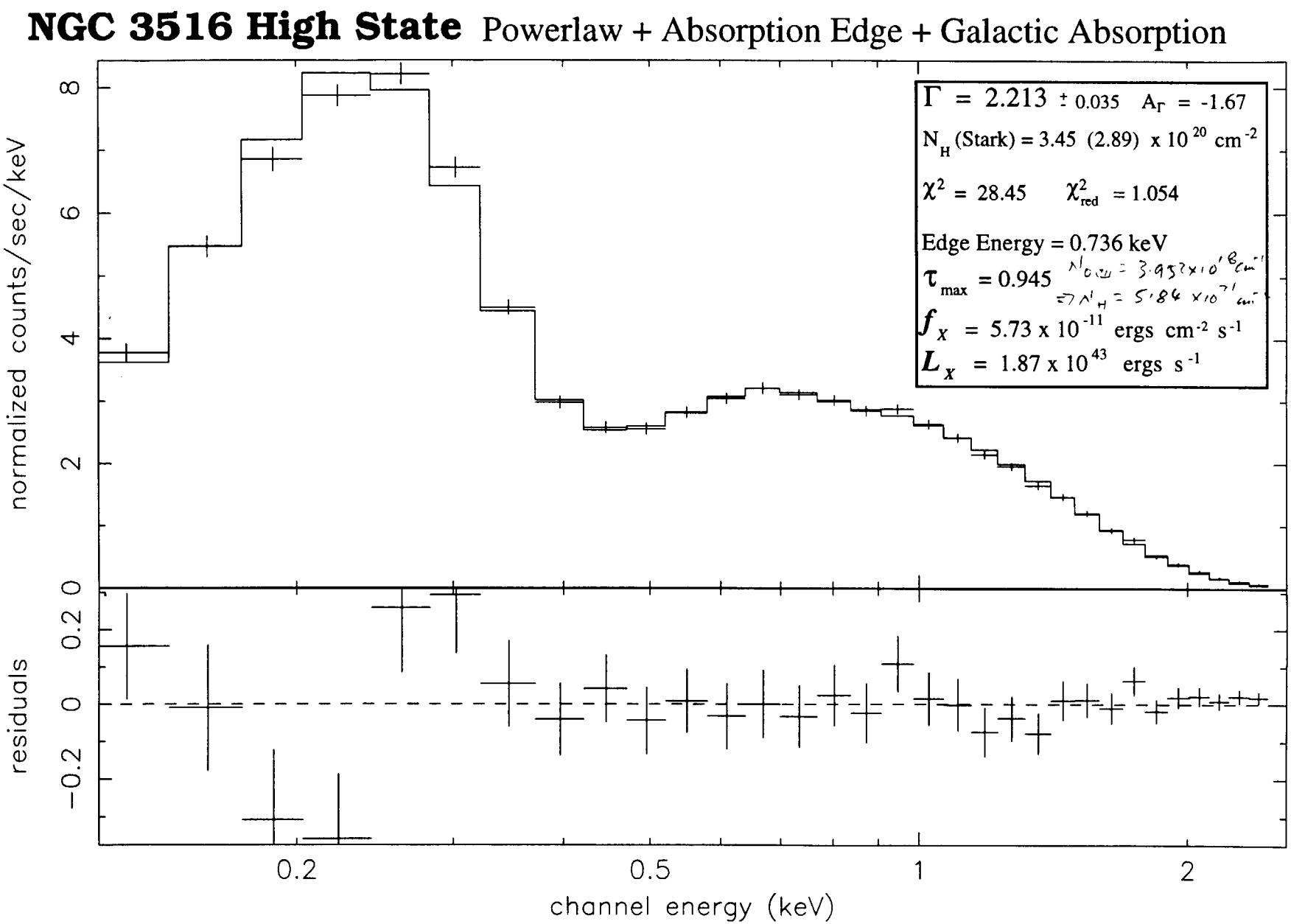
NGC 3516 High State Powerlaw + Absorption Edge + Galactic Absorption
Γ = 2.213 ± 0.035 A_Γ = -1.67
N_H (Stark) = 3.45 (2.89) x 10^20 cm^-2
χ^2 = 28.45 χ^2_red = 1.054
Edge Energy = 0.736 keV
τ_max = 0.945
f_X = 5.73 x 10^-11 ergs cm^-2 s^-1
L_X = 1.87 x 10^43 ergs s^-1
normalized counts/sec/keV
residuals
channel energy (keV)
0.2
0.5
1
2

Fig. 27

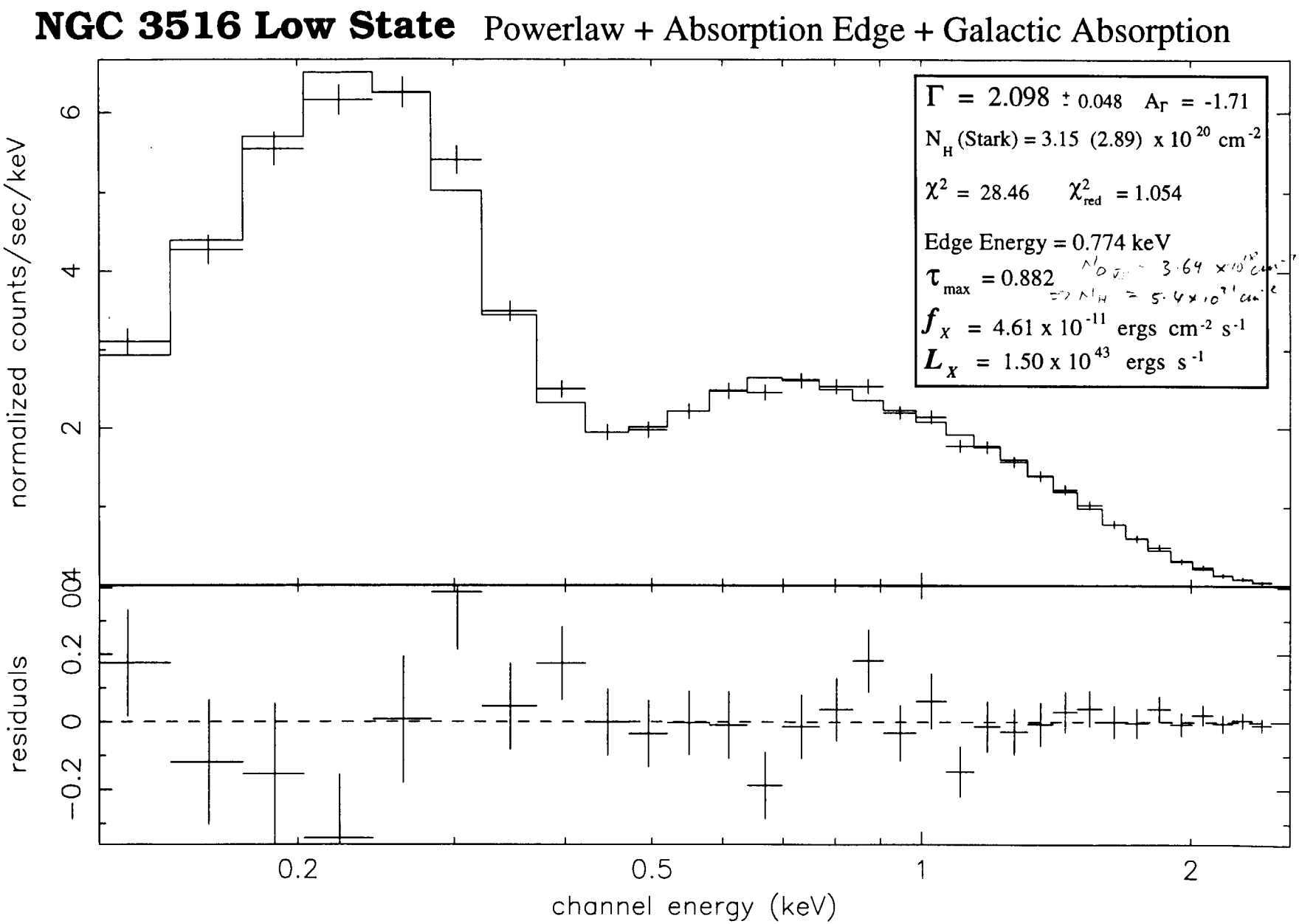
NGC 3516 Low State Powerlaw + Absorption Edge + Galactic Absorption
Γ = 2.098 ± 0.048 A_Γ = -1.71
N_H (Stark) = 3.15 (2.89) x 10^20 cm^-2
χ^2 = 28.46 χ^2_red = 1.054
Edge Energy = 0.774 keV
τ_max = 0.882
f_X = 4.61 x 10^-11 ergs cm^-2 s^-1
L_X = 1.50 x 10^43 ergs s^-1
normalized counts/sec/keV
residuals
channel energy (keV)
0.2
0.5
1
2

Fig. 28

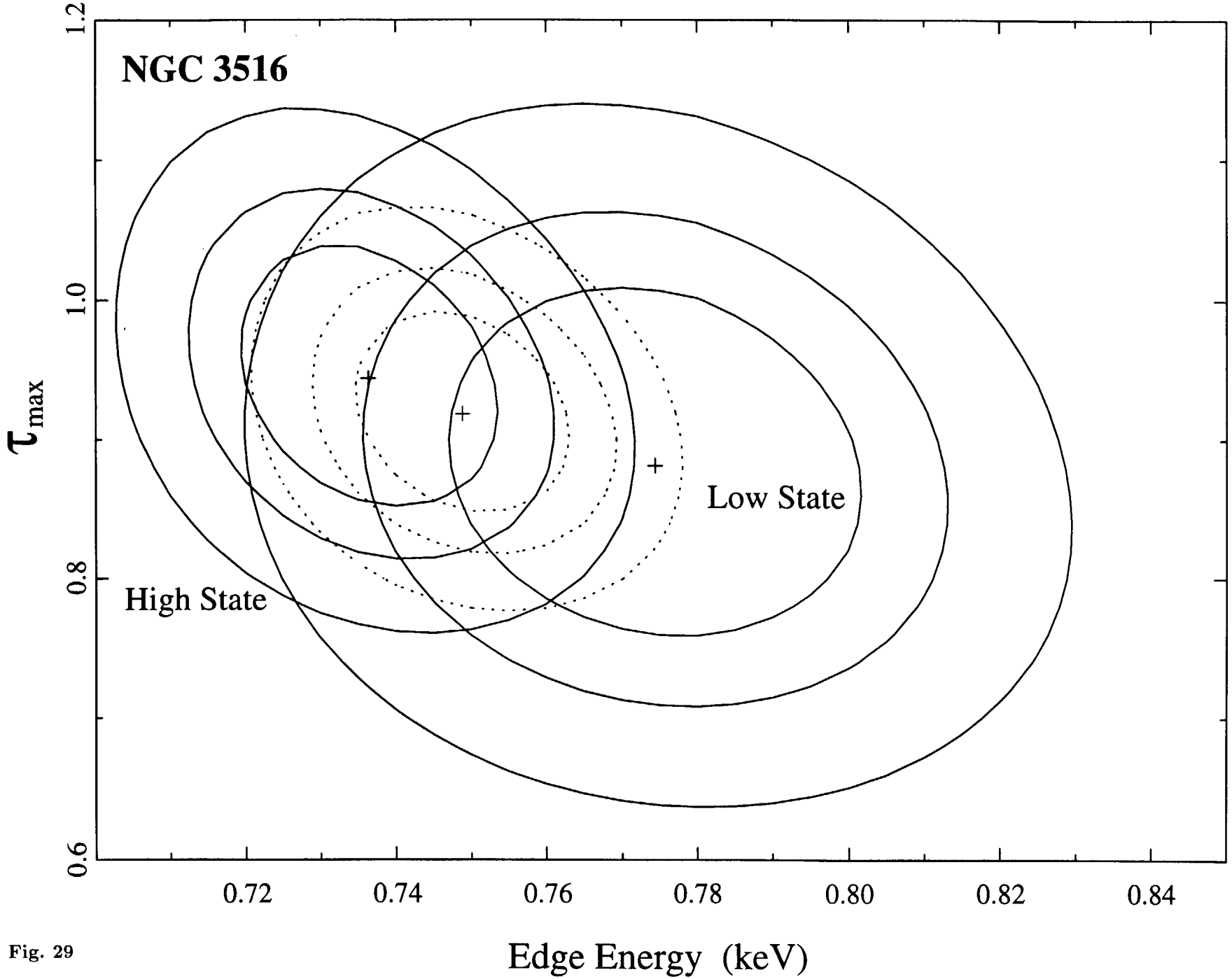
NGC 3516
High State
Low State
τ_{max}
1.2
1.0
0.8
0.6
0.72
0.74
0.76
0.78
0.80
0.82
0.84
Edge Energy (keV)

Fig. 29

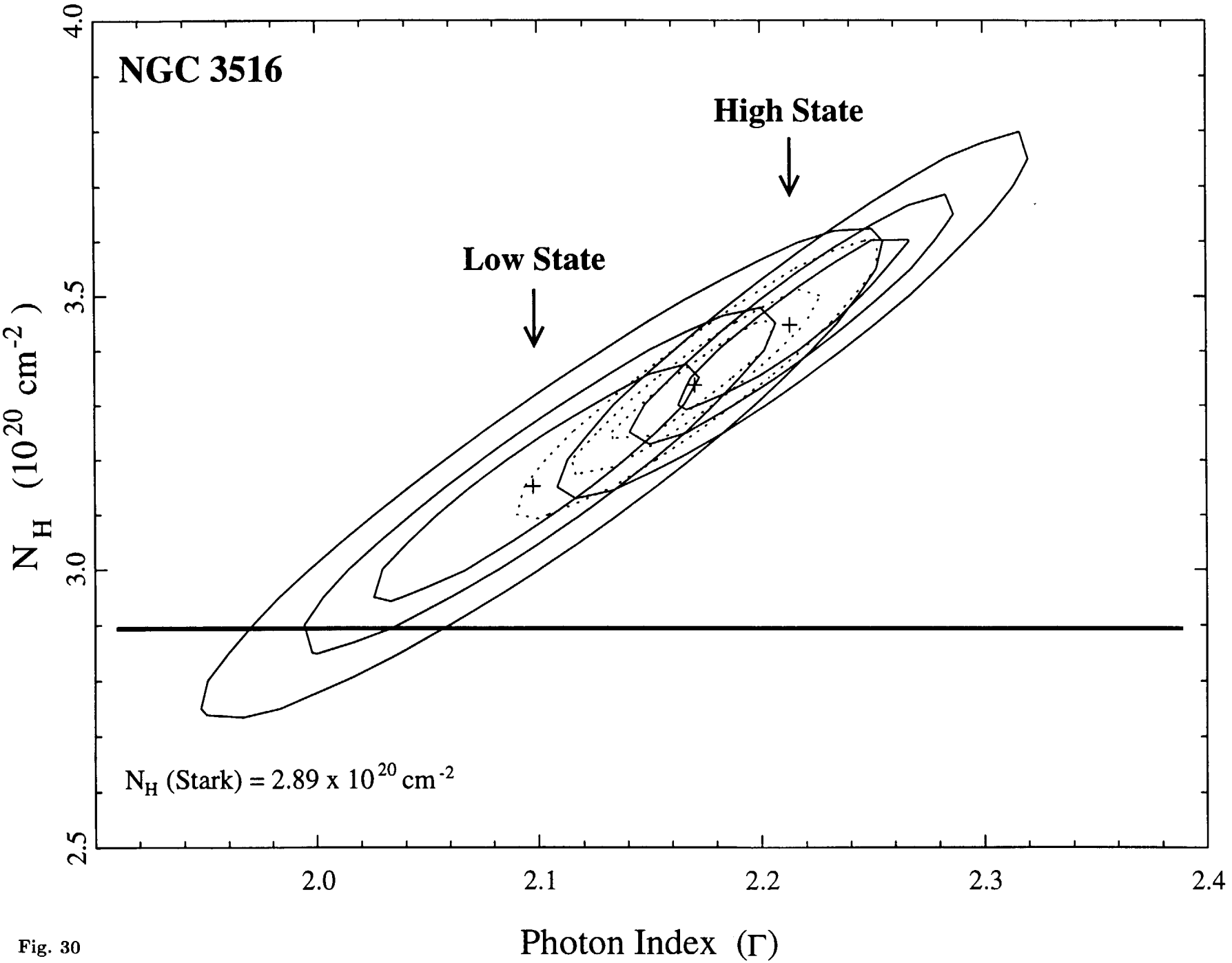
NGC 3516
High State
Low State
N_H (10^{20} cm^{-2})
4.0
3.5
3.0
2.5
N_H (Stark) = 2.89 x 10^{20} cm^{-2}
2.0
2.1
2.2
2.3
2.4
Photon Index (Γ)

Fig. 30

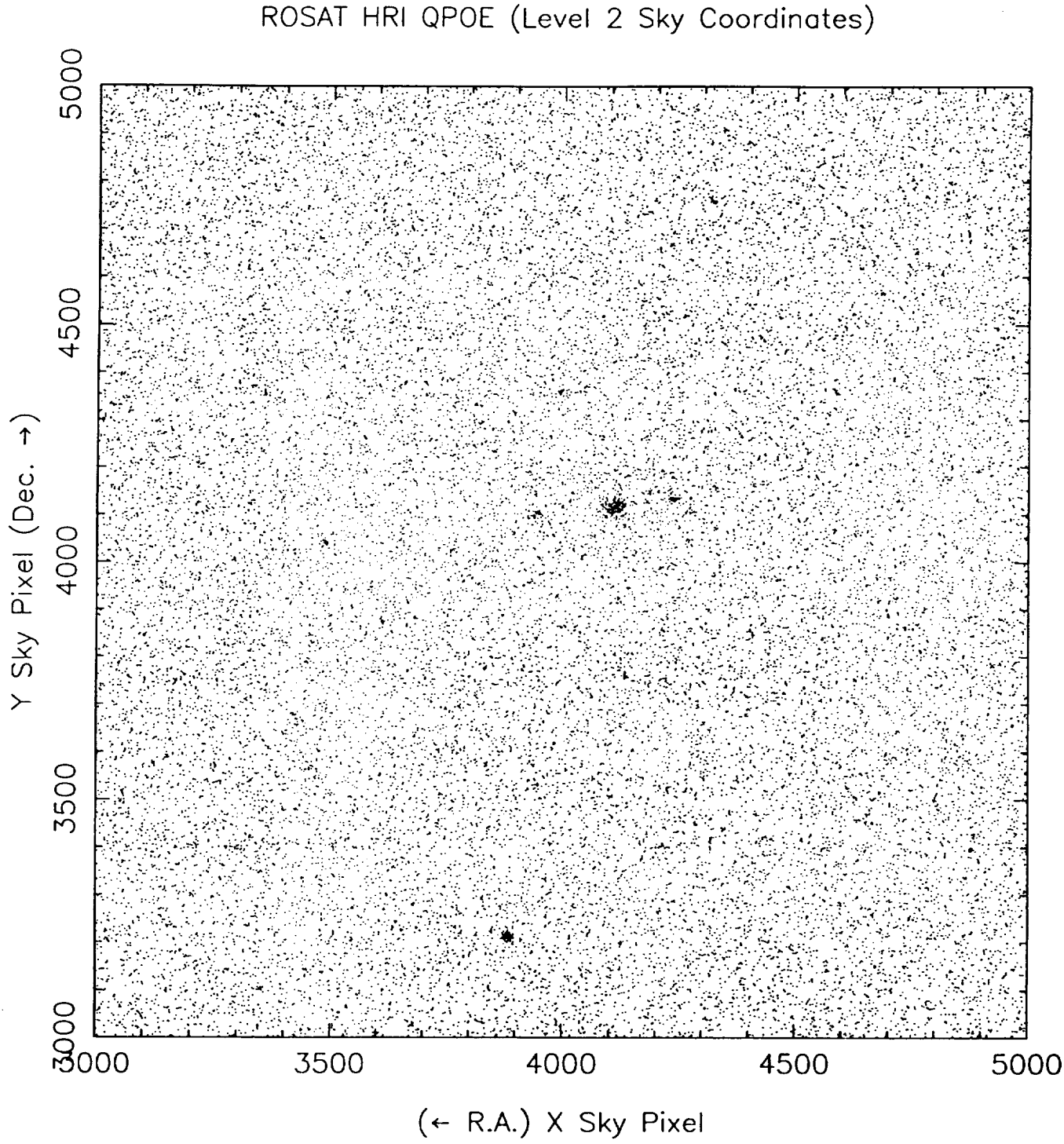
ROSAT HRI QPOE (Level 2 Sky Coordinates)
Y Sky Pixel (Dec. →)
(← R.A.) X Sky Pixel
3000
3500
4000
4500
5000

Fig. 31

APPENDIX

Papers Published Under NASA Grant NAG 5-1935

"The True Nature of *IRAS*-Selected, X-ray–Luminous "Normal" Galaxies in the *ROSAT* All-Sky Survey," Moran, E. C., Halpern, J. P., & Helfand, D. J. 1994, *Ap.J. (Letters)*, **433**, L65.

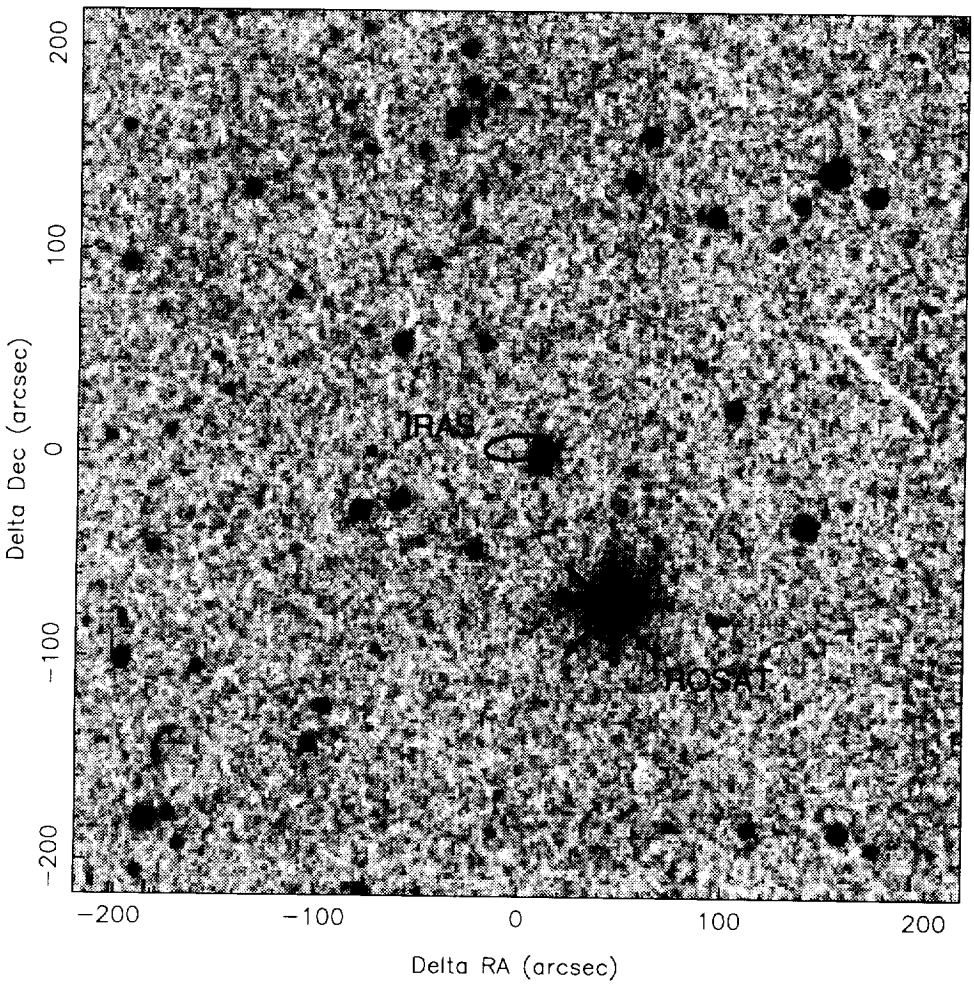

FIG. 2.—Optical finding chart for IRAS 16137+3618, made from the digitized POSS plates at STScI, with the *IRAS* error ellipse (95%) and the position of the RASS source marked (*cross*). The bright star ($m_V = 10.06$) coincident with the RASS position—not the H II *IRAS* galaxy—is virtually certain to be the X-ray source in this case. The *IRAS* error ellipse is centered at $\alpha_{2000} = 16^h15^m35^s.8$, $\delta_{2000} = +36^\circ10'48''$.

THE ASTROPHYSICAL JOURNAL, 433:L65–L68, 1994 October 1

THE TRUE NATURE OF *IRAS*-SELECTED, X-RAY–LUMINOUS "NORMAL" GALAXIES IN THE *ROSAT* ALL-SKY SURVEY

EDWARD C. MORAN,[1] JULES P. HALPERN,[1] AND DAVID J. HELFAND[1]
Department of Astronomy, Columbia University, 538 West 120th Street, New York, NY 10027
E-mail: ed@falstaff.phys.columbia.edu
Received 1994 May 25; accepted 1994 July 12

ABSTRACT

Luminous star-forming galaxies have often been suggested as potentially significant contributors to the cosmic X-ray background (XRB). Interest in this possibility has been rekindled by a recently published sample of 244 *IRAS/ROSAT* galaxies that includes 20 with extreme X-ray luminosities ($L_X = 10^{42-44}$ ergs s^{-1}) that are claimed to be "normal" spiral galaxies. To investigate whether or not these 20 X-ray–luminous spirals are truly normal star-forming galaxies, we have reexamined their classifications by obtaining new optical spectra of 13 of them, and by locating spectra in the literature for four. Our results indicate that 13 of the 17 objects are previously unrecognized Seyfert galaxies. Of the four star-forming non-Seyfert galaxies found in this sample, three are incorrectly identified as X-ray sources. Only one H II galaxy is a confirmed X-ray source, but it has $L_X \approx 10^{42}$ ergs s^{-1} and is only about twice as luminous as the most luminous normal spirals detected previously at X-ray wavelengths. Thus, there are no H II galaxies with L_X substantially in excess of 10^{42} ergs s^{-1}, and claims of a new class of X-ray–luminous spiral galaxies are not supported by this study.

Subject headings: galaxies: Seyfert — galaxies: starburst — X-rays: galaxies

1. INTRODUCTION

The cosmic X-ray background (XRB) is thought to originate from the integrated emission of discrete sources. The main weakness of this explanation is, however, that the characteristic spectra of known classes of extragalactic X-ray emitters are all considerably softer than the spectrum of the XRB itself. Since active galactic nuclei (AGNs) are the dominant class of extragalactic X-ray sources at high fluxes, it is commonly believed that they are responsible for the vast majority of the XRB. However, the space density and correlation length scale of AGNs, in addition to their typical broad-band X-ray spectra, are incompatible with an XRB origin in which AGNs contribute more than $\sim 50\%$ of the 2–10 keV flux (Fabian & Barcons 1992, and references therein). Furthermore, the best estimate to date of the soft X-ray luminosity function of AGNs (Boyle et al. 1993) rules out AGNs producing all of the XRB below 2 keV.

The contribution of star-forming galaxies to the XRB has been frequently considered, at both soft and hard X-ray energies (Persic et al. 1989; Griffiths & Padovani 1990; Lonsdale & Harmon 1991; Fruscione & Griffiths 1991; Rephaeli et al. 1991; Green, Anderson, & Ward 1992; David, Jones, & Forman 1992). The most plausible scenario for such a contribution, suggested by Griffiths & Padovani (1990), proposes that galaxies undergoing bursts of star formation in regions of low metallicity could spawn enough luminous high-mass X-ray binaries to have both high-integrated X-ray luminosities ($> 10^{42}$ ergs s^{-1}) and spectra well matched to the spectrum of the XRB. Possible examples of such starburst galaxies have surfaced in a recently published study of infrared- and X-ray–selected galaxies, which has claimed to find a new class of X-ray–luminous, "normal" (non-AGN) galaxies (Boller et al. 1992). In this *Letter* we present the results of our investigation of these allegedly normal spiral galaxies with extreme X-ray luminosities.

2. SAMPLE SELECTION AND OBSERVATIONS

The targets for this study were selected from Boller et al. (1992), who cross-correlated the *ROSAT* All-Sky Survey (RASS) with the *IRAS* Point Source Catalog (PSC). A total of 244 *IRAS* galaxies were found to be positionally coincident with *ROSAT* X-ray sources (within 100″). Optical identifications and classifications for most of these objects were found in the NASA/IPAC Extragalactic Database (NED). For 104 galaxies with published redshifts, the X-ray luminosity L_X in the 0.1–2.4 keV band was determined. Surprisingly, 20 of the 67 galaxies for which L_X exceeds 10^{42} ergs s^{-1} were reported as normal spirals or starbursts, despite X-ray luminosities that are characteristic of Seyfert galaxies. These 20 objects, with L_X ranging from $\sim 2 \times 10^{42}$ to $\sim 3 \times 10^{44}$ ergs s^{-1}, are several to several hundred times more luminous than the brightest spirals observed with the *Einstein Observatory*, and two to four orders of magnitude more luminous than typical spiral galaxies (Fabbiano 1989). Such remarkable high-energy luminosities represent a challenge to our current understanding of the production of X-rays in ordinary spirals. If their classifications are correct, the existence of high-L_X normal galaxies bears important implications for the problem of the XRB. An important first step toward understanding the true nature of the 20 X-ray–luminous spirals must be reliable spectroscopic classification.

We observed 13 high-L_X *IRAS/ROSAT* galaxies, primarily using the KPNO 2.1 m telescope and Goldcam CCD spectrograph, but also with the Shane 3 m telescope and Kast spectrograph at Lick Observatory and with the CTIO 4 m telescope and RC spectrograph. The spectra have sufficient resolution (4–7 Å full width at half-maximum [FWHM]) and wavelength coverage (most extend from ~ 3700 to 7400 Å) to allow us to

[1] Visiting Astronomer, Kitt Peak National Observatory, National Optical Astronomy Observatories, which is operated by AURA, Inc., under a cooperative agreement with the National Science Foundation.

TABLE 1

THE HIGH L_X SAMPLE

IRAS Name	Other	z	log L_X (ergs s^{-1})	$\Delta_{o/X}$	Classification	Reference	Comments
01161+1443	UGC 838	0.0229	42.25	66″	H II	1	Possible chance coincidence
01590−3158	Fairall 1077	0.0463	42.70	14	...		...
06280+6342	UCG 3478	0.0123	42.84	79	Sey 1	2	Possible chance coincidence
10126+7339	NGC 3147	0.0096	42.25	8	Sey 2	1, 3	FWHM ([N II], Hα) ≈ 400 km s^{-1}
10257−4338	NGC 3256	0.0090	42.27	9	H II	4	...
11353−4854	...	0.0172	42.73	17	Sey 1.9	1	...
11395+1033	NGC 3822	0.0203	42.27	34	Sey 2	1	FWHM ([N II], Hα) ≈ 400 km s^{-1}
12323−3659	...	0.0302	42.91	4	Sey 2	1	Line widths = 440–480 km s^{-1}
12393+3520	NGC 4619	0.0231	42.81	5	Sey 1	1	Weak, broad Hα
13218−1929	...	0.0172	42.47	13	Sey 1.9	1	...
13224−3809	...	0.0667	44.26	34	Sey 1	5	...
14288+5255	...	0.0449	42.45	16	Sey 2	1	Line widths = 415 km s^{-1}
15083+6825	...	0.0582	43.07	11	Sey 1.8	1	...
15374−1817	MCG − 03-04-004	0.0235	42.41	20	Sey 1	6	...
15564+6359	Kaz 49	0.0300	42.83	12	Sey 1.9	1, 7	Weak, broad Hα component, FWHM = 1150 km s^{-1}
16137+3618	...	0.0919	...	85	H II	1	Chance coincidence with star
16155+6831	IC 1215	0.0251	...	69	H II	1	No longer in RASS
17104−7305	...	0.0172	42.75	50	...		...
19463−5843	...	0.0540	44.26	38	...		...
21582+1018	Mrk 520	0.0268	42.56	60	Sey 1.9	1, 8	Possible chance coincidence

REFERENCES.—(1) This *Letter*; (2) de Grijp et al. 1992; (3) Kennicutt 1992; (4) Armus et al. 1989; (5) Boller et al. 1993; (6) Kirhakos & Steiner 1990; (7) Yegiazarian & Khachikian 1988; (8) Lonsdale et al. 1992.

classify accurately each object. For four additional high-L_X spirals, we found spectra in the literature sufficient for accurate classification, bringing the total number of object classifications reexamined here to 17.

3. SPECTROSCOPIC CLASSIFICATION

The classification of an emission-line galaxy depends on the velocity widths and intensity ratios of the emission lines observed in its optical spectrum. Unfortunately, there is no single prescription for this task; therefore, we adopt the following guidelines. Emission lines broader than ~300 km s^{-1} FWHM—too broad to result solely from a spiral galaxy rotation curve, and indicative, therefore, of a massive object in the nucleus—earn a galaxy an AGN classification. A galaxy whose emission-line flux ratios indicate that the ionizing continuum is harder than that produced by hot stars (Veilleux & Osterbrock 1987; Filippenko & Terlevich 1992) is also classified as an AGN, regardless of its line widths. We require that an object exhibit both narrow emission lines and H II region–like line flux ratios to be classified as an H II galaxy. Herein we refer to all non-AGN spiral galaxies (starbursts and more quiescent star-forming galaxies) collectively as H II galaxies, placing emphasis on the common mechanism powering their emission lines—hot stars—rather than their star formation rates.

Table 1 summarizes the available spectroscopic data, our classification and its basis, and the relevant references for each of the high-L_X galaxies. Our new optical spectra are displayed in Figure 1.We find that 13 objects are, in fact, AGNs; the remaining four are indeed H II galaxies with putative X-ray luminosities in excess of 10^{42} ergs s^{-1}. However, as we discuss below, the identification of three of these H II galaxies with *ROSAT* X-ray sources is doubtful.

4. CHANCE COINCIDENCES

Boller et al. included in their sample all cases for which the *IRAS*/*ROSAT* position offset is less than 100″ and acknowledged that a fraction of the IR/X-ray coincidences must arise by chance. The distribution of optical/X-ray position offsets (very similar to the distribution of IR/X-ray offsets) provides the best means for determining which entries in the sample are likely to be chance coincidences. RASS sources are located within 20″ of their optical counterparts 70% of the time (Brinkmann, Siebert, & Boller 1994); thus, only one genuine identification in the entire Boller et al. sample of 244 should have an optical/X-ray offset $\Delta_{o/X}$ as large as 60″, assuming the true distribution of $\Delta_{o/X}$ is Gaussian. Among the 20 high-L_X spirals, *five* have $\Delta_{o/X} > 60''$. Either the chance coincidences are concentrated in this subsample, or there are other systematics affecting the Boller et al. RASS X-ray source positions. Table 1 lists the values of $\Delta_{o/X}$ for each high-L_X galaxy.

IRAS 16137+3618, which we observed to be an H II galaxy (Fig. 1*j*), is a clear example of a chance coincidence. Figure 2 (Plate L2) displays the optical finding chart with the *IRAS* error ellipse and the RASS source position marked. Assuming this to be a real IR/X-ray match, Boller et al. reported that $L_X = 3 \times 10^{43}$ ergs s^{-1} for this H II galaxy. Notice, however, that the RASS source position falls directly on a bright star ($m_V = 10.06$) 85″ away from the galaxy. The star is virtually certain to be the X-ray source. Two of the AGNs, UGC 3478 and Mrk 520, and one H II galaxy, UGC 838, have $\Delta_{o/X} = 79''$, 60″, and 66″, respectively. If these are also chance coincidences, the total number is consistent with the Boller et al. estimate that the chance coincidence rate for the high-L_X spirals should be 20%. For the final large $\Delta_{o/X}$ object, IRAS 16155+6831 (an H II galaxy), we have learned (T. Boller 1994, private communication) that the X-ray source has been deleted from the X-ray catalog following a more recent processing of the RASS data.

5. DISCUSSION

To summarize our census of 17 of the 20 high-L_X "normal" spiral galaxies in the Boller et al. sample of X-ray–selected *IRAS* galaxies, we find that 13 are actually AGNs. Four others are H II galaxies. However, two of these H II galaxies are incor-

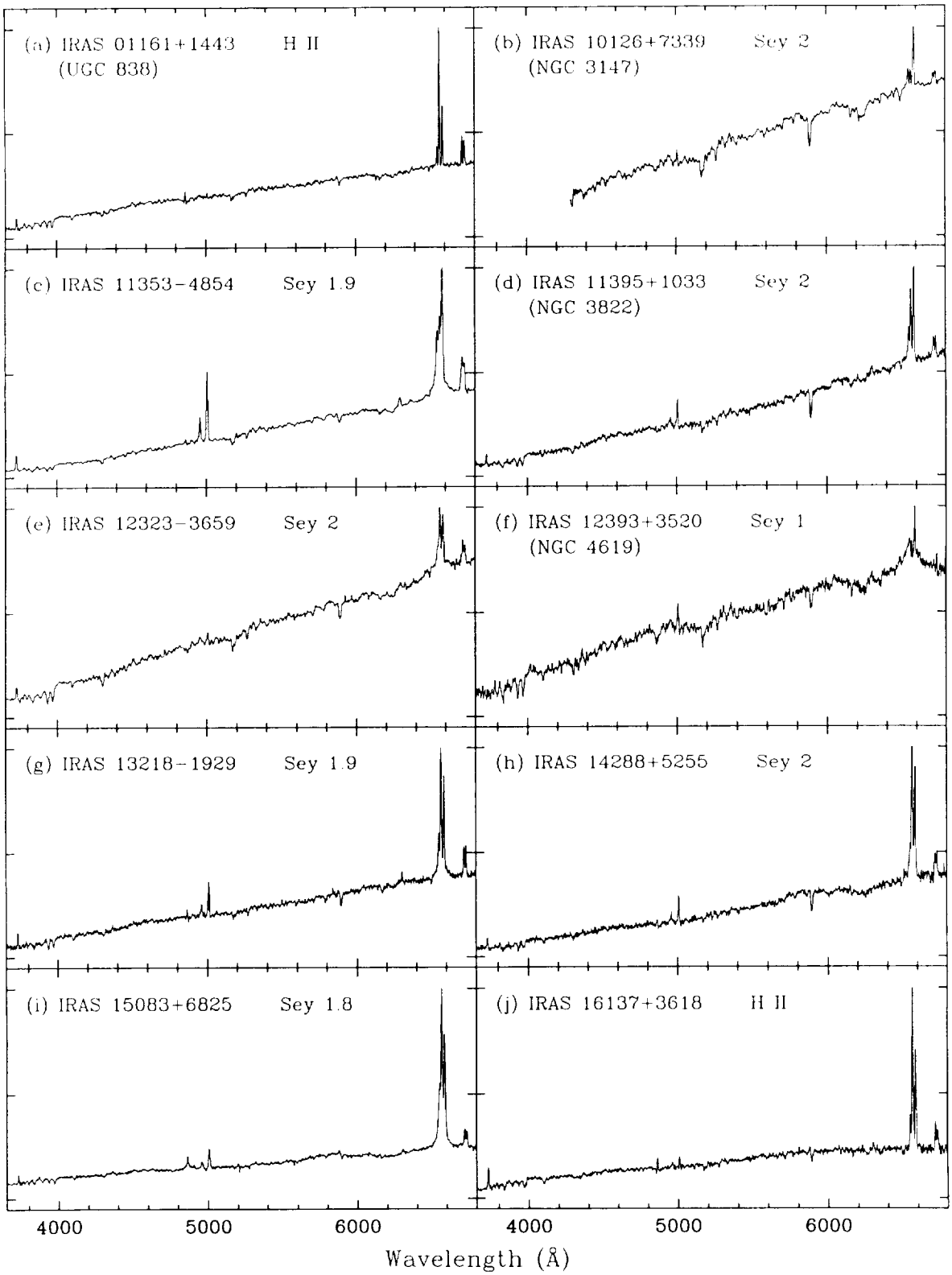

FIG. 1.—New spectra of 10 of the high-L_X galaxies. All but two [(*a*) and (*j*)] are AGNs. The vertical scales, in units of ergs cm^{-2} s^{-1} Hz^{-1}, have been normalized to unity. Not shown are our spectra of *IRAS* 16155+6831 (not an RASS source), Mrk 520 (Sey 1.9 spectrum published by Lonsdale et al. 1992), and Kaz 49 (Sey 1.9 spectrum published by Yegiazarian & Khachikian 1988).

rectly identified as X-ray sources, and the X-ray source originally associated with a third is not found in the current version of the RASS. Two of the AGNs may be also incorrectly identified as X-ray sources given their large $\Delta_{o/X}$ values. Thus, misclassifications, chance coincidences, and other errors are largely responsible for creating the illusion that a high fraction of the objects in the Boller et al. sample are normal galaxies with extreme X-ray luminosities.

Objects in the literature, and therefore in NED, have been classified for a variety of purposes using methods which differ in quality and accuracy. Thus, NED cannot be relied upon as the sole resource for establishing new classes of objects such as the high-L_X spirals. Perusal of the spectra in Figure 1 immediately reveals that several objects have Seyfert properties that are quite subtle. It is no surprise that these were previously misclassified as normal galaxies. The most dramatic case is that of NGC 3147. Kennicutt (1992) included this galaxy in his atlas as an example of a typical Sb spiral. Indeed, the emission lines in the integrated light spectrum are narrow with H II region-like ratios, since most of the emission line flux arises in extranuclear H II regions. The nuclear spectrum, however, indicates a strongly inverted [N II]/Hα ratio (only partially affected by a stellar Hα absorption feature) and broad [N II] lines (FWHM = 404 km s^{-1}). NGC 3147 is almost face-on, so lines this broad must arise in an active nucleus, which, although optically weak, is likely to be responsible for most of the X-ray emission from this object.

In the case of NGC 3256, the sole high-L_X H II galaxy for which the identification with a *ROSAT* X-ray source is secure, $L_X = 2 \times 10^{42}$ ergs s^{-1}. This is not substantially greater than highest X-ray luminosities known previously for H II galaxies (several 10^{41} ergs s^{-1}; Fabbiano, Kim, & Trinchieri 1992). *All* of the objects with $L_X > 3 \times 10^{42}$ ergs s^{-1} have turned out to be Seyfert galaxies. This result stands even if the H II galaxy UGC 838 is an RASS source, since it would have $L_X = 1.8 \times 10^{42}$ ergs s^{-1}. Thus, we conclude that NGC 3256 is probably a resident of the high-luminosity tail of the X-ray luminosity function for normal H II galaxies rather than a representative of a new class of X-ray–luminous spirals. These conclusions are supported by our larger followup study (Moran et al. 1994) of the unclassified members of the Boller et al. sample. All 51 objects observed to date are AGNs, stars, or H II galaxies with $L_X < 10^{42}$ ergs s^{-1}.

The sources of X-rays in normal spiral galaxies consist of accreting low- and high-mass X-ray binaries, supernova remnants, diffuse emission from the hot phase of the interstellar medium, and stars (Fabbiano 1989). If the X-ray emission in NGC 3256 arises due to these same sources in a combination similar to that in lower luminosity spirals, luminous H II galaxies such as this will have little impact on the XRB puzzle: their X-ray spectra would be too soft to contribute much flux to the background above ~ 3 keV, where the spectra of known classes of X-ray emitters and that of the XRB are most discrepant. Analysis of the broad-band X-ray spectrum of NGC 3256 obtained by *ASCA* will settle this question (Moran & Helfand 1994). Despite these discouraging prospects, the picture for a significant contribution to the XRB by H II galaxies as painted by Griffiths & Padovani (1990) cannot be ruled out. The soft X-ray selection of the Boller et al. sample might easily miss H II galaxies with large amounts of intrinsic absorption and, therefore, hard emitted spectra. With the exception of a handful of quasars, all the classified Boller et al. objects we know of (>150) have modest redshifts ($z < 0.15$) due to the sensitivity limits of the *IRAS* PSC and the RASS from which they were drawn; thus, the possibility of a population of star-forming galaxies at moderate redshifts with different spectral properties remains. X-ray images deeper than the RASS will have to be used to probe for X-ray-luminous H II galaxies at earlier epochs.

We are extremely grateful to Bob Becker and Mike Eracleous for obtaining the Lick and CTIO spectra presented here. This is Columbia Astrophysics Laboratory contribution 524.

REFERENCES

Armus, L., Heckman, T. M., & Miley, G. K. 1989, ApJ, 347, 727
Boller, T., Meurs, E. J. A., Brinkmann, W., Fink, H., Zimmermann, U., & Adorf, H.-M. 1992, A&A, 261, 57
Boller, T., Trumper, J., Melendi, S., Fink, H., Schaeidt, S., Caulet, A., & Dennefeld, M. 1993, A&A, 279, 53
Boyle, B. J., Griffiths, R. E., Shanks, T., Stewart, G. C., & Georgantopoulos, I. 1993, MNRAS, 260, 49
Brinkmann, W., Siebert, J., & Boller, T. 1994, A&A, 281, 355
David, L. P., Jones, C., & Forman, W. 1992, ApJ, 388, 82
De Grijp, M. H. K., Keel, W. C., Miley, G. K., Goudfrooij, P., & Lub, J. 1992, A&AS, 96, 389
Fabbiano, G. 1989, ARA&A, 27, 87
Fabbiano, G., Kim, D.-W., & Trinchieri, G. 1992, ApJS, 80, 531
Fabian, A. C., & Barcons, X. 1992, ARA&A, 30, 429
Filippenko, A. V., & Terlevich, R. 1992, ApJ, 397, L79
Fruscione, A., & Griffiths, R. E. 1991, ApJ, 380, L13
Green, P. J., Anderson, S. F., & Ward, M. J. 1993, MNRAS, 254, 30
Griffiths, R. E., & Padovani, P. 1990, ApJ, 360, 483
Kennicutt, R. C., Jr. 1992, ApJ, 388, 310
Kirhakos, S. D., & Steiner, J. E. 1990, AJ, 99, 1722
Lonsdale, C., & Harmon, R. 1991, Adv. Space Res., 11, 333
Moran, E. C., Halpern, J. P., & Helfand, D. J. 1994, in preparation
Moran, E. C., & Helfand, D. J. 1994, in preparation
Persic, M., et al. 1989, ApJ, 344, 125
Rephaeli, Y., Gruber, D., Persic, M., & MacDonald, D. 1991, ApJ, 380, L59
Veilleux, S., & Osterbrock, D. E. 1987, ApJS, 63, 295
Yegiazarian, A. A., & Khachikian, E. Ye. 1988, Soob. Byuarkan Spets. Astrofiz. Obs., 60, 3